ELSEVIER

Journal of Fluids and Structures 19 (2004) 251–275

JOURNAL OF FLUIDS AND STRUCTURES

www.elsevier.nl/locate/jnlabr/yjfls

Impact flows and loads on ship-deck structures

M. Greco[a,*], M. Landrini[a], O.M. Faltinsen[b]

[a] *INSEAN, The Italian Ship Model Basin, Via di Vallerano 139, 00128 Rome, Italy*
[b] *Centre for Ships and Ocean Structures, NTNU, Trondheim, Norway*

Received 13 May 2003; accepted 10 December 2003

Abstract

The shipping of water on the deck of a vessel in head-sea conditions and zero-forward speed is investigated by experimental and numerical means. Through the experimental observations the main stages of the fluid-dynamic phenomenon are identified. For the considered conditions, water shipping initiates with water front overturning onto the deck, entrapping air, and then flowing along the initially dry deck up to impacting against vertical superstructures. Numerically, the water-on-deck phenomena are studied by considering a simplified two-dimensional flow problem. The theoretical model relies on the assumption of inviscid fluid in irrotational motion. Through comparison against experimental data, it is shown that the potential-flow model suffices to give a robust and efficient estimate of green-water loads until large breaking phenomena, usually following impact events, are observed. A boundary element method with piecewise-linear shape functions for geometry and boundary data is used for the numerical solution. The fluid–structure interaction is studied by coupling the nonlinear potential flow model with a linear Euler beam to represent a portion of the deck house under the action of the shipped water. The loading conditions related to violent fluid impacts and air-cushion effects are discussed. Upon considering realistic parameters, the occurrence of critical conditions for structural safety is discussed. The role of hydroelasticity is addressed in the case of fluid impacting against a vertical wall.

1. Introduction

The practical prediction of wave-induced ship motions and loads has reached a reliable degree of maturity since the 1970s, when the strip-theory codes became available (Salvesen et al., 1970). The need to estimate occurrence and severity of dangerous events, such as the massive shipping of water on the deck of vessels (*green water*), is not of minor importance but rational prediction tools are not yet available.

In the last decades, the research effort has been largely stressed in this field. Limiting ourselves to the case of stationary structures, experimentally, fundamental features of the water shipping due to regular incoming waves on a floating production storage and offloading (FPSO) unit (Ersdal and Kvitrud, 2000) have been identified by Buchner (1995, 2002). Tests with different bow and stern shapes have been performed. Irregular incoming wave conditions were considered in the experiments carried out by Stansberg and Karlsen (2001) and the evolution of the shipped water onto the deck has been investigated. On the numerical side, Buchner and Cozijn (1997) analyzed the bow deck wetness for moored ships, assuming a two-dimensional problem in the longitudinal ship direction. The fluid was assumed inviscid and in irrotational motion and the problem was solved through a boundary element method with collocation points inside the elements. They presented both numerical simulations and experiments for a simple prototype problem but no comparison between simulations and measurements was presented. Numerical difficulties were documented concerning

*Corresponding author. Tel.: +39-06-50-299343; fax: +39-06-5070619.
E-mail address: m.greco@insean.it (M. Greco).

0889-9746/$ - see front matter © 2003 Elsevier Ltd. All rights reserved.
doi:10.1016/j.jfluidstructs.2003.12.009

the evolution of the free surface-body contact point at the starting of the water shipping. Studies based on Navier–Stokes equations coupled with VOF technique for treating the free surface are presented by Fekken et al. (1999) and Kleefsman et al. (2002). The numerical method is applied to solve an "equivalent" dam-breaking problem whose characteristics are determined by tuning with the studied water shipping events in the case of a FPSO. This means that the coupling between in deck-out deck flows is not accounted for.

Our recent research activity, briefly summarized in the experimental work by Barcellona et al. (2003), is mainly aimed to a fuller understanding of the fluid dynamics involved in water-on-deck phenomena, and the ability to predict and control water-shipping events. In this paper, we focus our attention on the hydrodynamic loads and structural consequences connected with the water invading and flowing along the deck, and finally impacting against the deck house in the bow region of a ship with zero forward speed and restrained from moving, subjected to head-incoming waves.

Although the presently neglected ship motions affect the phenomenon, and further investigations are needed to deal the general case of a ship sailing through waves, the present case is of practical relevance to understand green-water events on FPSO units since they are moored ships used as oil platforms and therefore operating at zero-mean forward speed. Further, FPSO ships are weather-vaning, therefore head sea represents the most severe condition in terms of water-shipping occurrence. Moreover, while for smaller vessels the water-on-deck concern is mainly related to ship stability (e.g. the capsizing for fishing vessels), the safety of structures and superstructures along the deck, together with operatability on board, represent the main issues when dealing with FPSOs. In this framework, the present analysis is of relevant practical content.

The analysis is based on a synergic combination of experimental observations with numerical modelling. In the first part, a preliminary global understanding of the phenomenon is presented through experimental investigations. These allow to identify the main stages of the flow-field evolution. Each of these is of concern from a structural point of view, and will be further investigated in the second part of the paper, after the numerical modelling has been presented. Upon assuming realistic parameters for the ship structure, we define the criticality of the different flow stages and the reliability of the mathematical model to deal with. Finally, the role of hydroelasticity during deck-house impacts after water shipping is addressed.

2. Experimental background

2.1. Three-dimensional experiments

An experimental investigation on three different models including flow visualization, pressure pattern on the wetted deck and impact force on a deck-like structure is presented by Barcellona et al. (2003). Two mathematical hull forms and a model of the ESSO-Osaka tanker have been considered. Here, we report a few new flow visualizations about the model of the ESSO-Osaka tanker, in head-sea conditions, without forward speed and restrained from moving. The aim is highlighting the main flow features to the purpose of later discussion on the structural implications.

The adopted model of the ESSO-Osaka tanker has draft $D = 0.284$ m, length between the perpendiculars $L = 4.44$ m and beam $B = 0.74$ m. The tests have been carried out at the INSEAN Towing Tank 2 (length 220 m, breadth 9 m and depth 3.6 m).

The main incident wave parameters have been determined by considering FPSO ships and their usual operational conditions. In particular, FPSO water-on-deck accidents in the North Sea documented that the most interesting wavelengths are of order of the ship length. Several casualties occurred during full-loaded conditions (Ersdal and Kvitrud, 2000) when the effective freeboard is smaller than the nominal value. Therefore, to have realistic water heights relative to the deck for representative design conditions, the upper portion of the bow has a reduced freeboard, $f = 0.064$ m, resulting in the nondimensional parameters $D/L \simeq 0.064$, $B/L \simeq 0.166$ and $f/L \simeq 0.015$. The uppermost portion of the hull and the bow region of the deck have been made by transparent material to permit visualizations of the water running up along the bow, entering the deck and flowing against a vertical plexiglas plate to mimic a deck-house wall. A video camera has been used in combination with a mirror placed under the ship deck. Images are recorded with a frame rate of 30 Hz. In real cases, water shipping may be due either to a single large wave, or to the cumulative effect of a small number of events associated with wave groups approaching the ship. In the latter case, the first event is not necessarily the most severe one. In the present tests, water on deck occurs as a single event due to the ship interaction with the wave packet. In this way, we also avoid disturbances due to wave reflections from the tank walls. The incident wave packet results from the focusing of several wave components generated with suitable phase relationships, Rappi and Melville (1990). The wave spectrum and the focusing point along the tank represent the input data. In the present case, each component has the same amplitude a. A characteristic steepness $k_c a$ of the wave packet

can be defined by using the wavenumber k_c associated with the mean frequency f_c of the spectrum. In tests here reported, we have chosen $f_c = 0.6$ Hz and the frequency bandwidth $\Delta f = 0.4$ Hz, respectively. This gives a characteristic wavelength $\lambda_c = 2\pi k_c = 4.33\ \text{m} \simeq 0.98L$. The shortest and the longest wave components correspond to $\simeq 0.5L$ and to $\simeq 2.6L$, respectively. The focusing technique implemented is described by Barcellona et al. (2003). In that work, the wave steepness parameter $k_c a$ has been varied between 0.125 and 0.25. Here, we discuss only the case $k_c a = 0.15$.

Fig. 1 shows the interaction of the wave packet approaching the ship bow from left to right. After the water exceeded the freeboard, it enters the deck in a nonuniform manner because of the three-dimensionality of the hull form. In particular, the water initially plunges onto the deck at the fore portion of the bow (first frame). As time goes on, the water shipped in that region flows along the deck, while the freeboard is also exceeded along the ship sides (second frame). The maximum relative water height is reached and the forward-most portion of the ship bow appears totally submerged (third frame). The water flowing on the deck finally impacts against the vertical wall in a complex fashion, starting from the lateral sides, while the shipping of water slows down and ends (fourth frame).

The analysis of top- and bottom-view camera recordings highlights the formation of air entrapment during the early stages of the water shipping and allows for a more complete interpretation of the fluid-flow evolution during the initial stage. An example is given in Fig. 2. The perspective error connected with the use of a mirror-video camera combined system has not been corrected in these images. The time increases from left to right and from top to bottom.

When the water exceeds the freeboard, the fluid front plunges onto the deck, forming the air cavity. At the beginning, near the fore portion of the deck, a circular-shaped structure is observed (first frame), increasing as the time increases. In the second snapshot, this structure is characterized by an inner-darker region, where the deck has been already wetted, and an outer-lighter ring, where air is present. In the same frame, two tubular cavities can be observed along the bow sides, and have been colored in yellow to make them more evident. These are nonuniform, with thickness slowly reducing from the ship center-line on.

As the wave packet propagates downstream the hull, "fresh" water enters the deck along the bow sides, moving initially inward. Because of the symmetry of the phenomenon, the lateral water fronts approach each other in proximity of the ship center-line and are diverted outward by their mutual interaction. Result of this interaction is also the formation and growth of an inner blunt fluid structure. As time passes, this structure is fed by the water shipped laterally and moves along the deck toward the deck house. The last frame shows the structure of the water front before the impact against the vertical wall. It is worth stressing the nonuniform distribution of water height, with a maximum value occurring around the ship center-line.

The shipped water eventually impacts against the deck house-like structure, as shown in Fig. 3. The interaction starts from the lateral sides (cf. last frame of Fig. 1), and becomes more vigorous when the innermost portions of the water

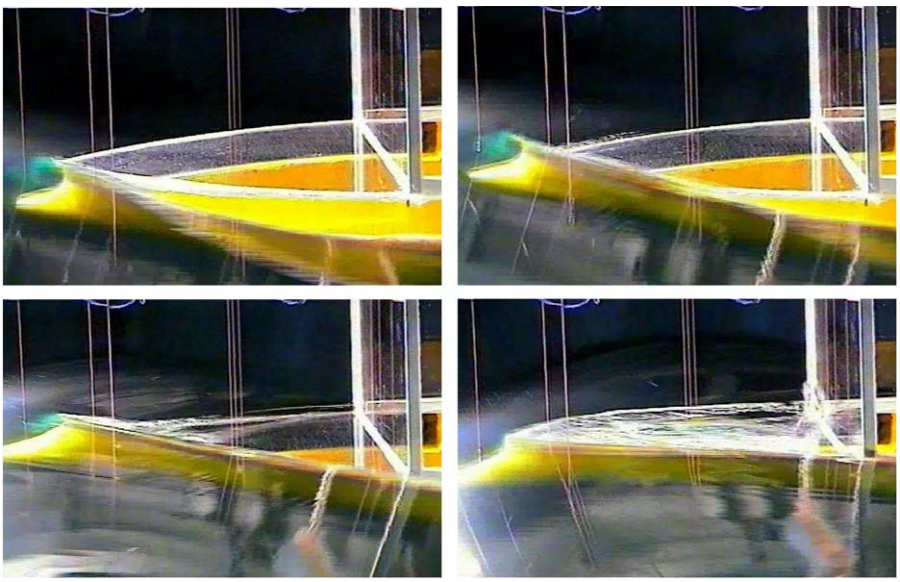

Fig. 1. Water shipping on ESSO-Osaka model induced by a wave packet ($k_c a = 0.15$ and $\lambda_c = 4.33$ m). Side view. The time increases from left to right and from top to bottom, with a time interval of 0.12 s.

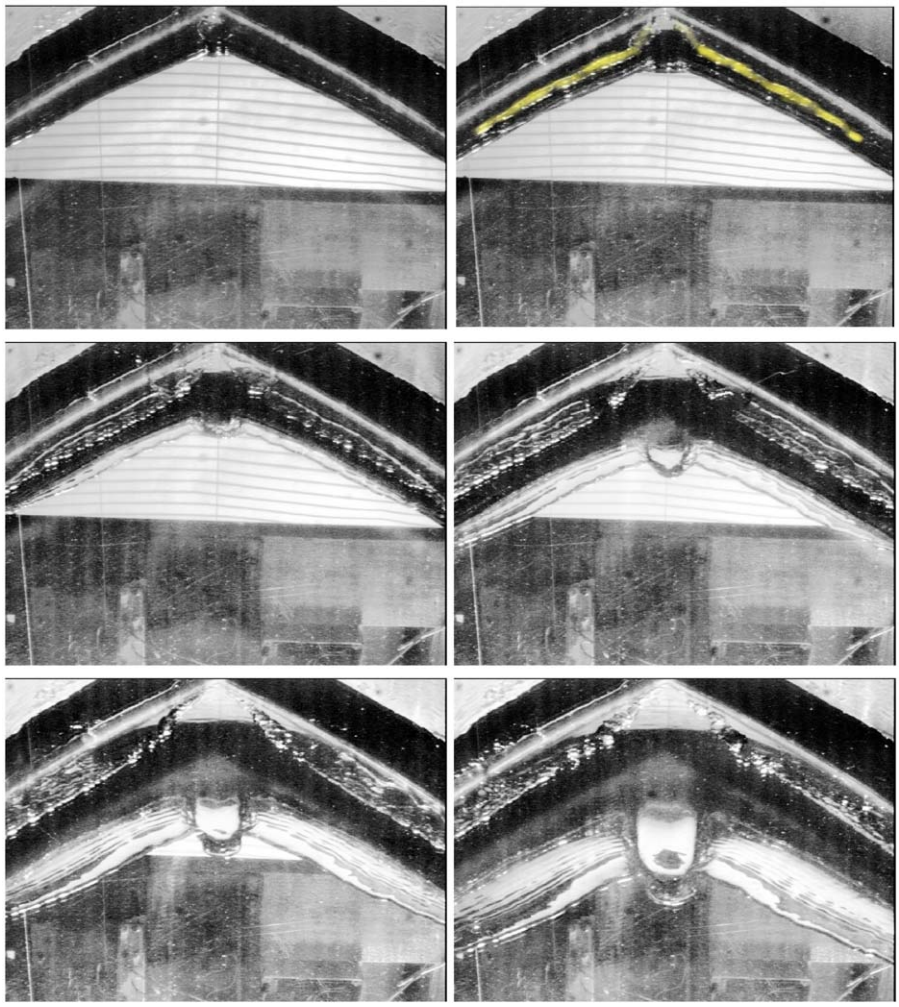

Fig. 2. Water shipping on ESSO-Osaka model induced by a wave packet ($k_c a = 0.15$ and $\lambda_c = 4.33$ m). Bottom view. The time increases from left to right and from top to bottom, with a time interval of $\simeq 0.033$ s. The water on deck starts in the form of a plunging wave from the fore portion of the bow (top-left), where the local wave elevation is higher. Then the freeboard is progressively exceeded along the ship side (top-right). The plunging wave entering the deck impacts with it and causes the formation of a cavity structure along the deck sides. Then, a water flow along the deck is generated with increasing velocity. This is characterized by a faster central tongue of fluid becoming wider as the time increases. Under the weight of the newly water invading the deck and partially convected by the main flow along the deck, the cavity collapses into bubbles. The visible horizontal black lines in the first four frames are the bottom-mirror reflection of the lines drawn on a panel in front of the bow and have not physical meaning.

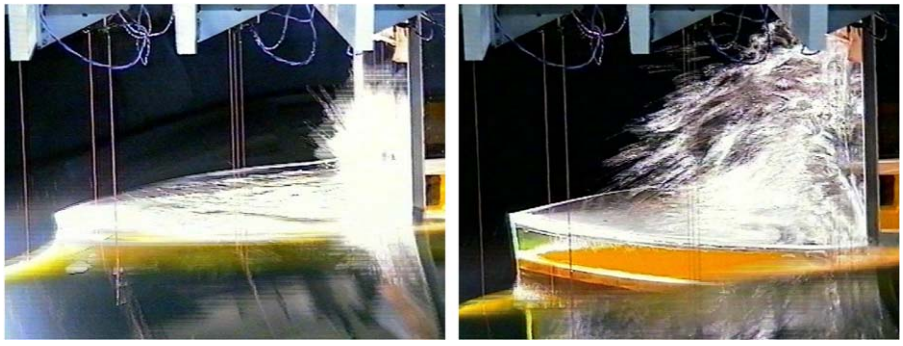

Fig. 3. Interaction of the shipped water with the vertical wall.

front, characterized by higher water height, reach the wall. After the maximum run up is reached, the fluid motion reverses backward, overturning onto the deck.

2.2. Two-dimensional laboratory tests

A clearer understanding of the water-shipping dynamics has been gained through two-dimensional water-on-deck laboratory tests, performed in the wave flume (length 13 m, depth 1 m and width 0.6 m) at the NTNU Department of Marine Hydrodynamics (Fig. 4). In this case, the flow field is simpler than that observed in the three-dimensional model-tests recalled before and therefore better suited for guiding and validating the numerical method discussed in the following. In the experiments, incoming waves are generated by a flap wave-maker. The body parameters here considered are: draft $D = 0.2$ m, length $L = 1.5$ m, freeboard $f = 0.05$ m. The bottom corner at the model was rounded with a radius of curvature 0.08 m to avoid significant vortex shedding. Body motions are restrained. Since the generated wave system is highly transient, with the first crest generally steeper than the following ones, we decided to focus our study on the first water-shipping event.

The fundamental stages of the water shipping and the interaction with the deck first, and with the superstructure then are described in Figs. 5–7.

In particular, Fig. 5 reports the enlarged view of the water front entering the deck. The shipping of the fluid initiates with water plunging directly onto the deck, cf. the top-left frame. This is similar as observed in the three-dimensional experiments. At this stage, high impact pressures are expected. After the impact, a cavity entrapping air is formed, as shown in the top-right and following frames. The changes of the cavity volume due to the motion of the surrounding fluid determine time-varying loads on the deck. This phase of the fluid–structure interaction may damage the deck at least if the air in the cavity cannot escape. The latter occurs more easily in three-dimensional conditions rather than in the two-dimensional flow field here considered.

After a time short with respect to the duration of the entire water-shipping, the gross features of the flow field resemble those originated after the breaking of a dam, as shown in Fig. 6. Namely, a tongue of fluid develops along the deck, without evidence of overturning of the water front. Therefore, the gross fluid dynamics is rather simple, with loads practically hydrostatic in proximity of the water front. In this context, an additional important contribution to local loads would be given by ship motions, though not allowed in our experiments. Actually, numerical results show that there are important interactions between the flow on the deck and the flow field exterior to the vessel. This limits the similarity with dam-break flows and the practical possibility of using shallow-water models (Greco, 2001).

Finally, the impact against the vertical structure is observed (bottom frames in Fig. 6). In the following evolution, cf. Fig. 7, the fluid rises rapidly along the vertical wall. The fluid run up is slowed down by the action of the gravity, and the water front thickens. After the maximum run up has been reached, the water collapses downward, and a backward overturning is observed.

3. Two-dimensional numerical modelling

Further physical insight is gained by the numerical simulation of the previously described two-dimensional wave–flume experimental conditions. The physical assumptions are discussed and the corresponding mathematical problem is then stated. At first the model is described in the rigid-body case. Then, the fluid–structure coupling to account for hydroelastic effects during the impact is discussed.

3.1. General assumptions and statement of the mathematical problem

In practical cases, the Reynolds number of the flow is high. Therefore, for unseparated flows, the vorticity is concentrated in the thin boundary layer at the body boundary, and a potential-flow model can be used to quantitatively describe the main features of the flow field, including the wave evolution around the hull and the induced pressure distribution. Boundary-layer effects may be relevant also in case of thin fluid layers on solid boundaries, as in case of the water front propagating on the deck. Moreover, the edge of the ship deck may induce separation and large vortex shedding. In the present analysis, such phenomena are a priori neglected. In general, surface-tension effects are negligible because of the relatively large spatial scales involved in practical cases. However, high curvature of the free surface may exist at the body-free surface intersection and in plunging waves, and there surface tension may be relevant. With these premises, a potential-flow model is adopted and the ''heavy'' water-on-deck is analyzed by fully retaining nonlinearities associated with the motion of the fluid boundaries.

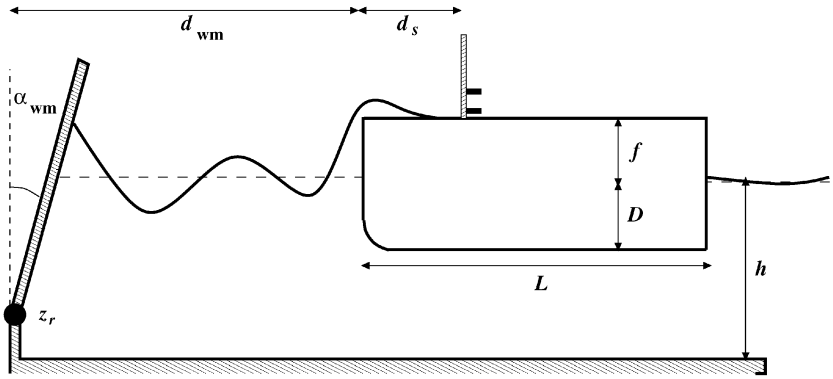

Fig. 4. Two-dimensional laboratory experiments: sketch of the set up and adopted nomenclature. Lengths are not in natural scale.

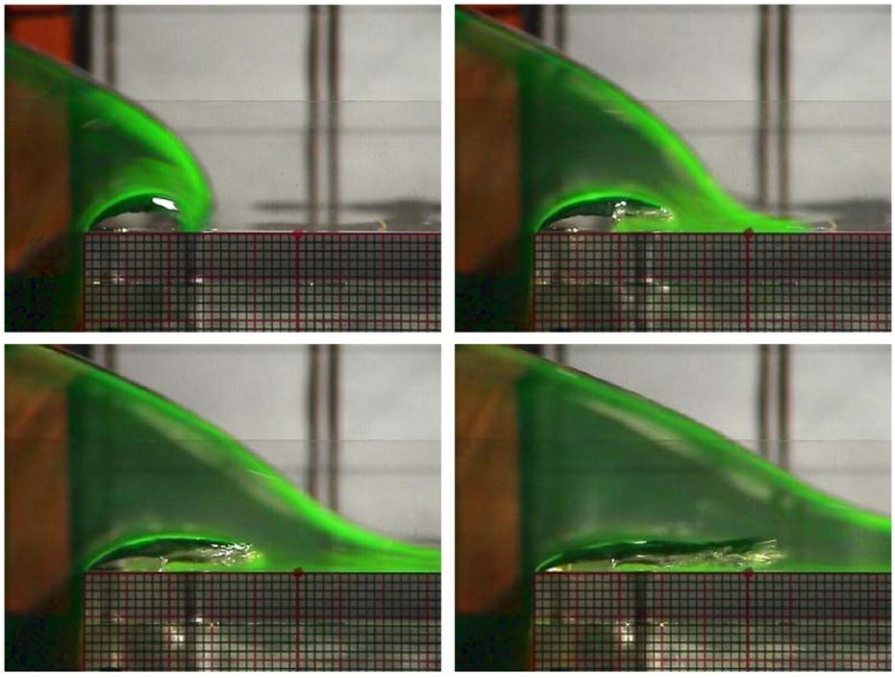

Fig. 5. Two-dimensional laboratory experiments ($\lambda/D = 10.1$, $H/D = 0.808$): initial stages of the water shipping. The water front plunges onto the deck forming an air pocket which is squeezed and stretched downstream by the main flow. Time increases from left to right and from top to bottom.

We consider the problem sketched in Fig. 8, where the fluid domain $\Omega(t)$ is bounded by the free surface $\partial\Omega_{FS}$, the wetted surface of a rigid body $\partial\Omega_{BO}$, and the outer surface $\partial\Omega_{\text{outer}}$ formed by the upstream portion containing the instantaneous wetted surface of the wave-maker and a straight horizontal bottom portion. The downstream longitudinal extension of the domain is taken large enough so that the fluid disturbance can be neglected, at least for finite time. The artificial dissipation of outgoing wave signals is discussed later. In general, the boundary $\partial\Omega$ of the fluid domain Ω varies with time.

We assume an incompressible and inviscid fluid in irrotational motion. A potential-flow model is therefore applicable. The velocity potential $\varphi(\boldsymbol{P}, t)$ satisfies the Laplace equation

$$\nabla^2 \varphi = 0 \tag{1}$$

everywhere in the fluid domain, and the fluid velocity is $\boldsymbol{u} = \nabla\varphi$.

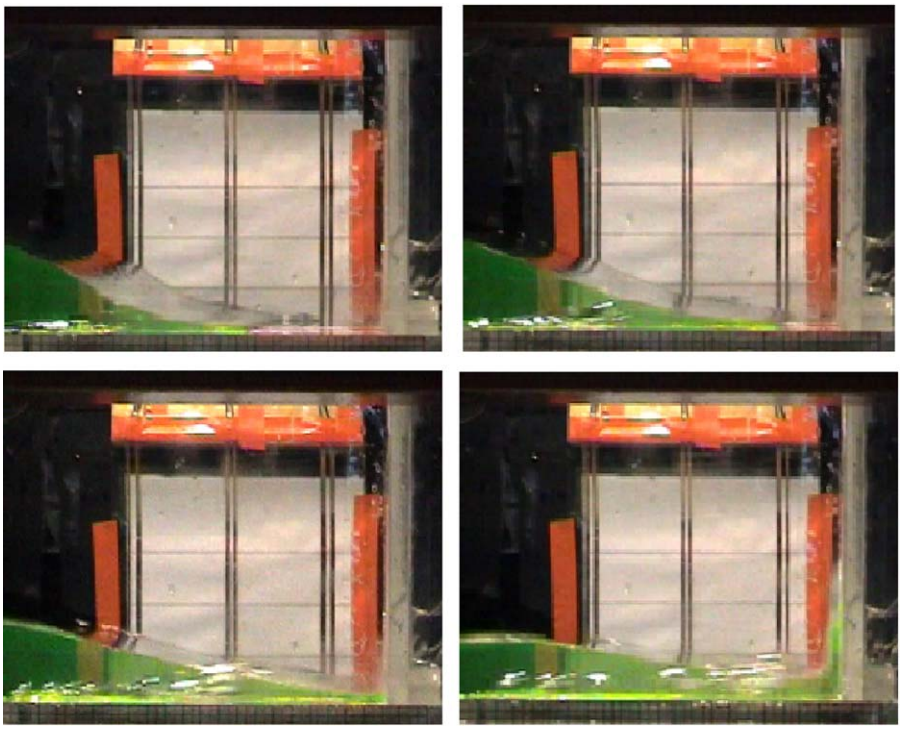

Fig. 6. Two-dimensional laboratory experiments ($\lambda/D = 10.1$, $H/D = 0.808$): late stages of the water shipping. A dam break-type flow develops along the deck. The water front eventually hits the vertical superstructure. Time increases from left to right and from top to bottom.

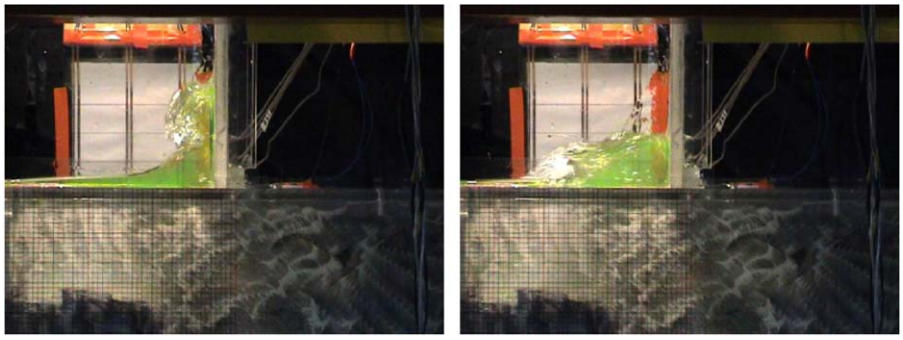

Fig. 7. Two-dimensional laboratory experiments ($\lambda/D = 10.1$, $H/D = 0.808$): late evolution of the impact against the vertical superstructure. After the maximum run-up the water plunges backward onto the deck.

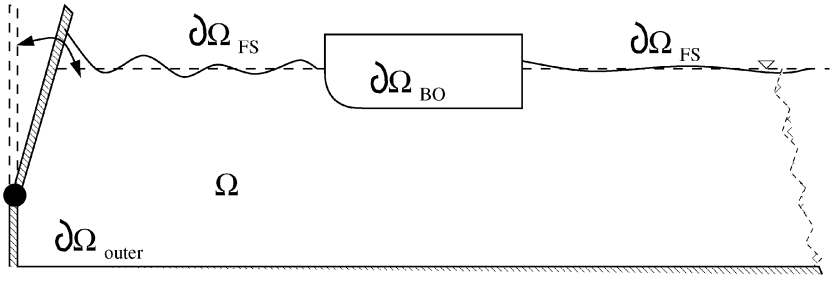

Fig. 8. Sketch of the numerical two-dimensional problem.

3.1.1. Conditions at the free surface

The free surface configuration and the velocity potential on the free surface at any time instant have to be found as a part of the numerical solution. This is achieved by enforcing the kinematic and dynamic conditions along this boundary portion, in combination with other boundary conditions, initial conditions and Laplace equation.

In particular, fluid particles cannot cross the free surface and, upon neglecting surface-tension effects, the pressure p at the free surface is balanced by the ambient pressure p_a, which is assumed constant. Therefore, through the Bernoulli equation and by using a Lagrangian description, we can write the free-surface conditions as

$$\frac{\mathrm{D}\boldsymbol{P}}{\mathrm{D}t} = \nabla\varphi, \quad \frac{\mathrm{D}\varphi}{\mathrm{D}t} = \frac{1}{2}|\nabla\varphi|^2 - g\eta - \frac{p_a}{\rho}, \quad \forall t,\ \forall \boldsymbol{P} \in \partial\Omega_{FS}, \tag{2}$$

where $\boldsymbol{P}$ is the location of a free-surface point, η is the corresponding wave elevation, and $\mathrm{D}/\mathrm{D}t = \partial/\partial t + \nabla\varphi \cdot \nabla$ is the total, or *material*, derivative. Eqs. (2) are well known and state that the free surface is made by fluid particles moving with the fluid velocity $\nabla\varphi$ and carrying a value of the potential φ which evolves according to the second equation.

3.1.2. Condition at rigid boundary

Fluid particles cannot cross the body boundary, and the corresponding kinematic condition reads

$$\frac{\partial\varphi}{\partial n} = \boldsymbol{V}_P \cdot \boldsymbol{n} \quad \forall t,\ \forall \boldsymbol{P} \in \partial\Omega/\partial\Omega_{FS}, \tag{3}$$

where $\boldsymbol{n}$ is the unit normal vector to the surface assumed pointing out of the fluid domain and $\boldsymbol{V}_P$ is the velocity of a point along the surface. In the considered cases, the body velocity is either zero or known a priori.

3.1.3. Pressure and hydrodynamic loads

The pressure can be computed by the Bernoulli equation,

$$p = p_e - \rho\left(\frac{\partial\varphi}{\partial t} + \frac{1}{2}|\nabla\varphi|^2 + gz\right) \tag{4}$$

and the force follows by direct pressure integration along surfaces of interest. The numerical evaluation of rate-of-change of the velocity potential $\partial\varphi/\partial t$ in (4) will be described later.

3.2. Numerical solution

We adopt the mixed Eulerian–Lagrangian method (Ogilvie, 1967; Longuett-Higgins and Cokelet, 1976; Faltinsen, 1977). Let us assume that, at a given instant of time t_0, the boundary geometry $\partial\Omega$ is known together with the velocity potential along the free surface, and the component of the velocity normal to impermeable boundaries. The problem is then solved by the following two-step procedure:

(i) A boundary value problem (b.v.p.) for the Laplace equation can be stated as

$$\begin{aligned} &\nabla^2\varphi = 0 \quad \forall \boldsymbol{P} \in \Omega, \\ &\varphi = f(\boldsymbol{P}) \quad \forall \boldsymbol{P} \in \partial\Omega_{\mathscr{D}}, \\ &\frac{\partial\varphi}{\partial n} = g(\boldsymbol{P}) \quad \forall \boldsymbol{P} \in \partial\Omega_{\mathscr{N}}. \end{aligned} \tag{5}$$

In general, the Dirichlet boundary $\partial\Omega_{\mathscr{D}}$ and the Neumann boundary $\partial\Omega_{\mathscr{N}}$ are only a subset of the domain boundary, since along some parts of $\partial\Omega$ both φ and its normal derivative can be known. In the present case, the portion $\partial\Omega_{\text{outer}} \cup \partial\Omega_{BO}$ of the boundary is of Neumann type, the free surface is a Dirichlet-type boundary and far downstream the body both φ and its normal gradient are assumed vanishingly small.

By solving the b.v.p. (5), we determine the fluid velocity, and (5) can be referred to as the "kinetic problem". This is also said to be the "Eulerian step" of the procedure because problem (5) is solved for a frozen configuration of the flow field.

As we will discuss later, at this stage the term $\partial\varphi/\partial t$, needed for the pressure evaluation, can also be calculated.

(ii) The kinematic and dynamic conditions giving, respectively, the evolution of the free-surface geometry and of the free-surface velocity potential can be stepped forward in time. If a Lagrangian formulation for the free surface is used this step can be properly defined as the "Lagrangian step" of the procedure.

The pressure along the instantaneous wetted surface of the body can be evaluated and the body motions, if not restrained, can be calculated.

This provides new values for the boundary data along the Dirichlet and the Neumann boundaries, and the procedure can be repeated at the new time instant from Step (i) above.

3.2.1. Kinetic problem

The kinetic problem (5) is recast in terms of boundary-integral equations, and solved by a boundary-element method (BEM). Features and drawbacks of using boundary-integral equations for free-surface flows have been discussed at length by many authors (see e.g. Yeung, 1982). We only mention that the simplicity of handling highly distorted configurations such those appearing during water shipping, formation of plunging waves, and impact against structures gives a decisive advantage over discretization-field methods, where a grid covering the whole fluid domain is required. On the other hand, the method cannot be applied to deal with the post-breaking evolution.

The necessary integral equations are obtained by using the Green's third identity:

$$\int_{\partial\Omega}\left(\varphi\frac{\partial G}{\partial n_Q}-\frac{\partial\varphi}{\partial n_Q}G\right)\mathrm{d}\ell_Q=\begin{cases}2\pi\varphi(\boldsymbol{P}), & \boldsymbol{P}\in\Omega,\\ 0, & \boldsymbol{P}\notin\partial\Omega\cup\Omega,\\ \theta(\boldsymbol{P})\varphi(\boldsymbol{P}), & \boldsymbol{P}\in\partial\Omega.\end{cases}\tag{6}$$

In (6), $\boldsymbol{Q}$ is a point on the domain boundary, $\boldsymbol{n}_Q$ is the unit vector normal to the boundary and pointing out of the fluid domain, and $G(\boldsymbol{P},\boldsymbol{Q})=\ln|\boldsymbol{P}-\boldsymbol{Q}|$ is the fundamental solution of the Laplace equation in the two-dimensional space R^2. Finally, θ is the inner angle (relative to the fluid domain) at point $\boldsymbol{P}$ along the boundary.

The integral representation (6) gives the velocity potential within the fluid domain, once φ and $\partial\varphi/\partial n$ are known along the boundary. Conversely, for points $\boldsymbol{P}$ on the boundary, (6) gives a compatibility condition on the boundary data. In particular, if only some of them are known we can write integral equations to determine the remaining unknown boundary data. In our case, we deal with boundary portions characterized by Dirichlet (free surface), Neumann (rigid bodies) or Robin (elastic bodies) conditions. The obtained integral equations are then discretized by dividing the boundary portions in a finite number of elements. This leads to a system of linear algebraic equations. More in detail, in the present implementation we adopt a panel method with piecewise-linear shape functions both for geometry and for boundary data, with collocation points at the edges of each element. This was preferred to higher-order schemes, e.g. Landrini et al. (1999), which may lead to numerical difficulties at the body-free surface intersection point. On the other hand, a lower-order method requires a finer discretization in regions with high curvature of the boundary. An accurate tracking of the free boundary is crucial in areas with high free-surface curvature, in particular to satisfy fluid-mass conservation. During the simulation, this has been achieved by inserting dynamically new points where appropriate.

Continuity of the velocity potential is assumed at those points where the free surface meets a solid boundary. Though no rigorous justification is available, this procedure gives convergence of the numerical results under grid refinement, Dommermuth and Yue (1987). Occasionally, when the contact angle becomes too small, numerical problems still may occur and the jet-like flow created during a water-entry phase is partially cut (Zhao and Faltinsen, 1993).

We remark that in a fully nonlinear simulation both the known terms and the matrix coefficients of the algebraic equations system have to be evaluated each time the geometry and the boundary data change.

Once the system has been solved, φ and its normal derivative become available along the whole boundary. The tangential velocity $\partial\varphi/\partial\tau$ along $\partial\Omega$ ($\boldsymbol{\tau}$ is the unit vector tangent to the boundary) is determined by using finite-difference operators. The velocity is then used for the Lagrangian tracking of the free surface, as described in Section 3.2.3.

3.2.2. Evaluation of $\partial\varphi/\partial t$

The evaluation of the pressure along the body-wetted surface $\partial\Omega_{BO}$ requires the rate-of-change $\partial\varphi/\partial t$ of the velocity potential. However, with moving boundaries (free surface and moving body boundary), the Eulerian derivative $\partial\varphi(\boldsymbol{P},t)/\partial t$ is not even defined because the point $\boldsymbol{P}$ on the considered boundary is changing in time. Therefore, some practical difficulties are expected.

Cointe (1989) observed that $\partial\varphi/\partial t$ is solution of the Laplace equation with a Dirichlet condition on the free surface following from the Bernoulli equation and a Neumann condition on the body boundary involving high-order derivatives of the fluid velocity along the body contour. The problem is formally equivalent to the kinetic problem for φ discussed above and the computation of $\partial\varphi/\partial t$ by BEM does not change significantly the computational effort. Moreover, in the present case, the boundary condition on the rigid boundaries reduces to a simple homogeneous condition.

3.2.3. Time integration

A standard fourth-order Runge–Kutta scheme is adopted to step forward in time the evolution equations associated with the problem. This method represents a good compromise between accuracy and computational costs. In particular, by a linear stability analysis (Colicchio and Landrini, 2003), it can be seen that the scheme becomes unstable only by using very large time steps Δt, which is never the case because the tracking of the physical dynamics of water shipping limits more severely the magnitude of Δt. Finally, the method results to be slightly dissipative. The dissipation rate decreases as the time step decreases, and for the global time scales here analyzed (of the order of few periods of the incoming wave) this is negligible.

The implementation details of the scheme are well known. In particular, it requires the solution of four kinetic problems for each physical time step due to the (fictitious) auxiliary intermediate time instants. For a linearized problem, this procedure would be equivalent to a fourth-order Taylor expansion in time with an error of $\mathcal{O}(\Delta t^5)$. Though less demanding schemes are conceivable, we adopted the described scheme because of the simplicity in changing dynamically the time step. This was found crucial to keep under control the accuracy of the solution during the development of jet flows, impacts, and breaking waves.

3.2.4. Absorbing boundary conditions

We will study water-on-deck induced by head-sea regular waves generated by a given motion of a wave-maker. The wave disturbances transmitted past the body may reach the edge of the computational domain within a time-scale smaller than that needed by the simulation. This can cause unphysical reflections and hamper the results.

To prevent this problem, a damping region is placed in proximity of the boundary domain downstream the body. This is achieved by introducing damping terms proportional to the elevation η and the potential φ in the free-surface conditions (Israeli and Orszag, 1989; Cointe, 1989; Clément, 1996), i.e.

$$\frac{\mathrm{D}\boldsymbol{P}}{\mathrm{D}t} = \nabla\varphi - \nu(\boldsymbol{P})\eta\boldsymbol{e}_z, \quad \frac{\mathrm{D}\varphi}{\mathrm{D}t} = \frac{1}{2}|\nabla\varphi|^2 - g\eta - \nu(\boldsymbol{P})\varphi, \quad \forall t,\ \forall \boldsymbol{P}\in\partial\Omega_{FS}, \tag{7}$$

where $\boldsymbol{e}_z$ is the unit vector along the z-axis.

To avoid reflections during the transition from the free-surface conditions (2) to the modified ones (7), the damping coefficient $\nu(\boldsymbol{P})$ starts from zero, smoothly increases within the free-surface portion $\mathscr{L}_1$ and then constantly keeps the maximum value $\nu_{\max}$ in the ending portion $\mathscr{L}_2$. In particular, we adopted the form

$$\nu(\boldsymbol{P}) = \begin{cases} 0 & \forall \boldsymbol{P}\in\partial\Omega_{FS}/\mathscr{L}_1\cup\mathscr{L}_2, \\ \nu_{\max}\left(-2\left(\dfrac{l}{l_1}\right)^3 + 3\left(\dfrac{l}{l_1}\right)^2\right) & \forall \boldsymbol{P}\in\mathscr{L}_1, \\ \nu_{\max} & \forall \boldsymbol{P}\in\mathscr{L}_2, \end{cases} \tag{8}$$

where ℓ is the horizontal coordinate of $\boldsymbol{P}\in\partial\Omega_{FS}$ from the beginning of the damping layer (cf. Fig. 9).

The length $l_1 + l_2$ of the damping layer and the value of $\nu_{\max}$ have to be empirically determined. In this work, l_1 has been chosen at least equal to twice the incoming wave length λ, while l_2 could be much larger to better damp out long-wave components. To the latter purpose, some stretching of the free-surface panels is introduced to obtain a stronger reduction of these long-wave components.

Finally, in the physical wave flume an automatic control system adjusts the wave-maker motion to absorb reflected waves and to ensure the desired wave conditions. We used the actual wave-maker motion during the experiments to

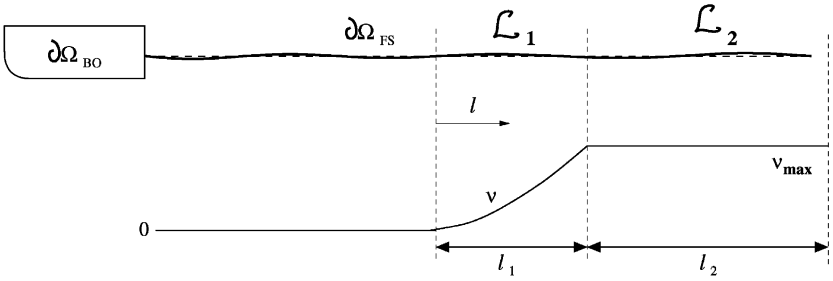

Fig. 9. Sketch of the numerical damping region.

drive our numerical wave-maker and absorption of reflected waves from the ship to the same degree as in the experiments is expected also in the simulations.

3.3. Modelling of the flow field during water shipping

A crucial aspect of the water-on-deck problem is represented by the prediction of the shipping occurrence. The behavior of the fluid flow when freeboard is exceeded represents a physical interesting and still rather unclear stage of the whole event. Therefore, numerical modelling has to rely upon experimental observations in the hope to grasp correctly the physics. As discussed, two-dimensional experiments have shown that water shipping initiates with the water front plunging onto the deck. The spatial scale involved is small (compared with the ship draft), and the time scale of the impact short with respect to the characteristic wave period. After the impact occurred, on spatial scales large with respect to the impact region, water propagation resembles that observed in dam break-type flows. On this ground, we devised two different local treatments to model the numerical solution at the edge of the deck.

3.3.1. Continuous Kutta-like condition

The very initial stage is modelled as shown in the left plot of Fig. 10. A Kutta-like condition similar to the Kutta condition applied in foil theory is enforced at the edge of the deck, corresponding here to the foil trailing edge. Such condition specifies that there is no cross-flow at the trailing edge. This implies that the flow leaves the foil surface tangentially at the trailing edge. By transferring this definition to the problem of interest, this means that we enforce the fluid to leave tangentially the bow edge during the whole evolution. Therefore, we named this as a "continuous" Kutta-like condition. Numerically this has been applied as follows. When the freeboard is reached, the contact point (CP) is left to proceed tangentially to the bow stem, and a new element is created with length $\partial\varphi/\partial\tau\Delta t$, $\boldsymbol{\tau}$ being the unit vector tangent to the bow stem, and carrying the current value of the potential at CP, which is treated as unknown in the integral equation. During the evolution, a new free-surface panel is created each time the size of the element nearest to the bow edge exceeds the mean size of the free-surface panels near the bow. Numerical simulations obtained by enforcing the continuous Kutta-like condition demonstrated to be successful in describing the formation of the water plunging onto the deck and its evolution until the water impact with the deck. Present method, based on a Boundary

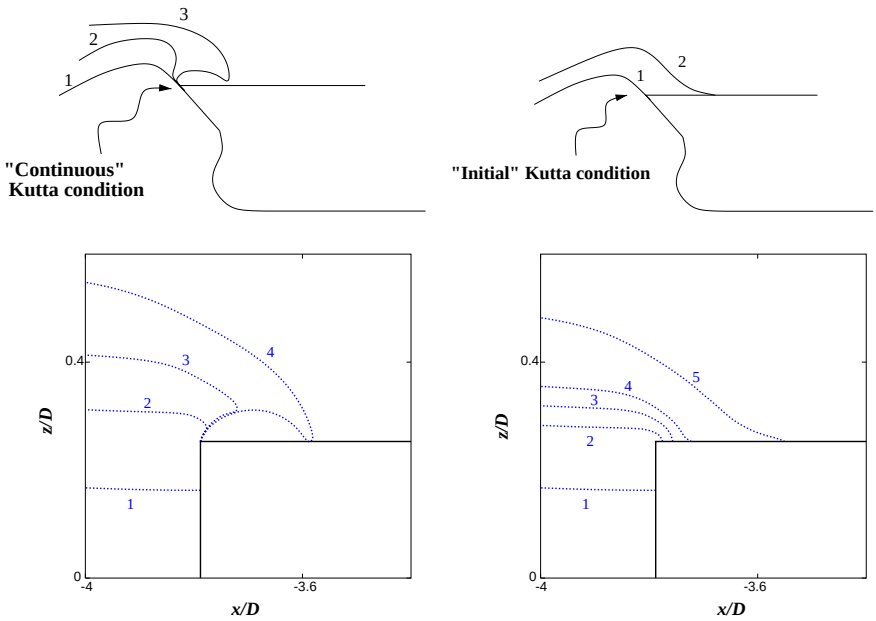

Fig. 10. Left: "Continuous" Kutta-like condition at the edge of the deck. Sketch (top plot) and example from numerical simulations (for a vertical bow, bottom plot) of the free surface evolution near the edge of the deck. The free surface configurations are enumerated as the time increases. Right: "Initial" Kutta-like condition at the edge of the deck. Sketch (top plot) and example from numerical simulations (for a vertical bow, bottom plot) of the free surface evolution near the edge of the deck. The free surface configurations are enumerated as the time increases.

Element Method, cannot handle the post-impact evolution and the numerical simulation is stopped when the free surface hits the solid boundary.

In the experiments we observed that, after the initial impact, the long-time evolution of the flow follows a dam break-like pattern. To study the water-on-deck phenomena occurring on this larger time scale, we decided to relax the condition at the edge of the deck applying what we named as the "initial" Kutta-like condition.

3.3.2. "Initial" Kutta-like condition

As sketched in the right plot of Fig. 10, when water reaches the instantaneous freeboard the fluid is enforced to leave tangentially the bow, thus a Kutta-like condition is initially applied. Once the freeboard is exceeded, the Kutta-like condition is not enforced anymore and the free-surface velocity relative to the ship determines whether the deck will be wetted or the water will be diverted in the opposite direction. If locally the relative free-surface velocity is favorable to the water entering the ship deck the fluid particle closest to the deck is allowed to move tangentially along it, causing deck wetness.

We verified a posteriori that this treatment allows a good prediction of water-on-deck occurrence, and captures efficiently the subsequent flow-field evolution along the deck.

To study the water shipping phenomena by enforcing the same (continuous Kutta-like) condition at the edge of the deck during the whole flow evolution, we need to handle the initial water-impact with the deck. This can be made for example by matching the numerical solution with a suitable local high-speed jet-flow solution. In this way it is also possible to study the evolution of the air cavity caused by the impact, before the cavity collapse in bubbles. This approach has not been presently attempted, yet.

3.4. Modelling of the hydroelastic problem

In some circumstances, the motion of the body boundary due to elastic deformations takes place on spatial scales and frequencies suitable to significantly influence the fluid motion. In this context, it is fundamental that the time scale of the considered fluid motion (loading time) is comparable with the dominant structural elastic natural periods, which in practice means the highest ones. When this occurs, the fluid-dynamic problem and the structural problem are coupled and have to be simultaneously solved (hydroelastic problem).

In the present context, when the shipped water hits structures along the deck, elastic deformations may have importance and influence the flow conditions. To assess the role of hydroelasticity, we need to formulate a hydroelastic model, that is the structural and fluid-dynamic problems have to be solved simultaneously.

The interaction of the shipped water impacting against a portion of the deck is studied in Section 4.3 by coupling the nonlinear potential-flow model with a linear Euler-beam model. The use of a rather simple structural model simplifies the resulting numerical modelling and the analysis. For a more realistic treatment, one should use more complicated structural models. However, main focus is to assess the importance of hydroelasticity for a stiffened flat steel panel, and the beam model adopted gives a satisfactory approximation for the considered structure. Small beam deformations are assumed and, consistently with the Euler-beam model, rotations of the beam sections are neglected. Finally, structural damping is assumed negligible. This assumption is proper for the lower natural modes which mostly matter in practice. On this ground, the adopted beam equation is

$$m\frac{\partial^2 w}{\partial t^2} + EI\frac{\partial^4 w}{\partial \xi^4} = p\left(\xi, w, \frac{\partial w}{\partial t}, \frac{\partial^2 w}{\partial t^2}\right) = -\rho\left(\frac{1}{2}|\nabla\varphi|^2 + \frac{\partial\varphi}{\partial t} - \boldsymbol{g}\cdot\boldsymbol{P}\right), \tag{9}$$

where $\boldsymbol{g}$ is the gravity acceleration, $\boldsymbol{P}$ is a point on the deformed beam, m is the structural mass per unit length, EI is the beam bending stiffness, where E is the Young modulus and I the area moment of inertia per unit width of the beam about the neutral axis. Specification of constraints at the beam edges provides two boundary conditions at each of them. In the right-hand side, it is emphasized that the deformation w is forced by the fluid pressure p which depends, through the Bernoulli equation, on the location ξ along the beam, and on the deformation and its first and second time derivatives.

Suppose that, at a given instant of time, the beam geometry w and the deformation velocity $\partial w/\partial t$ are known, together with the other suitable boundary data along free and rigid surfaces. Then the b.v.p. for the velocity potential φ can be solved by imposing the no-penetration condition:

$$\frac{\partial\varphi}{\partial n} = \frac{\partial w}{\partial t} \tag{10}$$

along the wetted portion of the beam, and the already stated conditions on the remaining boundary portions. The fluid velocity $\nabla\varphi$ can then be evaluated, in particular, along the beam.

To evaluate the hydrodynamic pressure forcing the beam $\partial\varphi/\partial t$ is also needed. Since $\partial\varphi/\partial t$ is a harmonic function, it can be found by solving a suitable b.v.p. for the Laplace equation $\nabla^2[\partial\varphi/\partial t] = 0$. The boundary condition on free and rigid boundaries can be derived in a similar way as already discussed. On the wetted portion of the beam, the boundary condition has the less common form of a nonhomogeneous Robin condition:

$$\frac{\partial}{\partial n}\left(\frac{\partial\varphi}{\partial t}\right) + \frac{\rho}{m}\frac{\partial\varphi}{\partial t} = a_1(\xi) + a_2(\xi). \tag{11}$$

Here ρ is the water density, m the structural mass per unit length and unit width of the beam and a_1 and a_2 are known functions of the longitudinal coordinate ξ given by

$$\begin{aligned} a_1 &= \frac{\partial w}{\partial t}\frac{\partial^2\varphi}{\partial\tau^2} - \frac{\partial\varphi}{\partial\tau}\frac{\partial^2 w}{\partial\xi\partial t}, \\ a_2 &= -\frac{1}{m}\left(EI\frac{\partial^4 w}{\partial\xi^4} + \rho\frac{1}{2}|\nabla\varphi|^2 - \rho\boldsymbol{g}\cdot\boldsymbol{P}\right). \end{aligned} \tag{12}$$

Eq. (11) follows by specifying that the acceleration of particles lying along the beam in the normal direction equals that of beam points, that is

$$\boldsymbol{n}\cdot\mathrm{D}\boldsymbol{u}/\mathrm{D}t = \partial^2 w/\partial t^2. \tag{13}$$

Here the assumption of linear beam theory has been used and higher-order terms with respect to the structural deformations have been neglected. By developing the left-hand side of Eq. (13) and introducing $\boldsymbol{n}$ and $\boldsymbol{\tau}$ as, respectively, unit normal and tangential vectors to the beam, we have

$$\begin{aligned} &\boldsymbol{n}\cdot\frac{\partial\nabla\varphi}{\partial t} + \boldsymbol{n}\cdot[\nabla\varphi\cdot\nabla(\nabla\varphi)] = \frac{\partial^2 w}{\partial t^2} \\ &\Rightarrow \frac{\partial^2\varphi}{\partial t\,\partial n} + \boldsymbol{n}\cdot\left\{\nabla\varphi\cdot\nabla\left[\frac{\partial\varphi}{\partial n}\boldsymbol{n} + \frac{\partial\varphi}{\partial\tau}\boldsymbol{\tau}\right]\right\} = \frac{\partial^2 w}{\partial t^2} \\ &\Rightarrow \frac{\partial}{\partial n}\left(\frac{\partial\varphi}{\partial t}\right) = -\frac{\partial\varphi}{\partial n}\frac{\partial^2\varphi}{\partial n^2} - \frac{\partial\varphi}{\partial\tau}\frac{\partial}{\partial\tau}\left(\frac{\partial\varphi}{\partial n}\right) + \frac{\partial^2 w}{\partial t^2}. \end{aligned}$$

Condition (11) is finally obtained, under the approximation of linear beam theory, once introduced in the last expression condition (10) for $\partial\varphi/\partial n$, the Laplace equation for $\partial^2\varphi/\partial n^2$, and the beam equation (9) for $\partial^2 w/\partial t^2$.

We observe that the b.v.p. for $\partial\varphi/\partial t$ is not formally the same as the problem for φ. A second set of integral equations has therefore to be solved, increasing the computational effort.

For the spatial discretization of (9), the transverse deformation $w(\xi, t)$ is approximated as a (truncated) series

$$w(\xi, t) \simeq \sum_{j=1}^{N} \zeta_j(t)\,\Psi_j(\xi) \tag{14}$$

in terms of N dry modes $\Psi_j(\xi)$ of the beam, which can be analytically determined according to the specific boundary conditions at the beam ends. The corresponding modal amplitudes $\zeta_j(t)$ are the unknowns of the problem. By projecting Eq. (9) along the basis $\{\Psi_j\}$, we obtain a set of ordinary differential equations for the time evolution of $\zeta_j(t)$. The equations are hydrodynamically coupled each other, i.e. through $\int p(\xi, w, \ldots)\Psi_j(\xi)\,\mathrm{d}\xi$.

Once the fluid pressure is known, fluid motion and structural deformation can be updated in time. The wetted portion of the beam at the next time instant is directly obtained once the evolution of the free surface-structure intersection point has been evaluated.

A procedure, similar to the one discussed above, has been introduced by Tanizawa (1999) to analyze the impact of a flexible body with the free surface.

In spite of the linearized structural model, in the computations the beam geometry is actually deformed according to $w(\xi, t)$ since it was found numerically preferable to satisfy the boundary condition on the instantaneous beam position. This has been made since in the fluid-dynamic problem the free surface evolution is nonlinearly analyzed. Using the instantaneous beam position allowed for a more stable prediction of the beam-free surface intersection, which can be difficult during the run-up stage when the contact angle can be very small.

No stability problems have been encountered for the time evolution of the beam equation (9) despite the added mass terms (i.e. terms depending on the acceleration) are not identified in the right-hand side and moved in the left-hand side. This is due to the use of an explicit fluid–structure coupling by means of the beam Robin boundary condition for $\partial\varphi/\partial t$.

Differently, stability problems have been documented in the case of hydroelastic analyses using iterative approaches to enforce the fluid–structure coupling when the added masses terms are left on the right-hand side of Eq. (9), see e.g. Kvålsvold (1994).

4. Analysis of the fluid–structure interaction

In the following, the structural implications of the fluid–structure interaction associated with the shipping of water are investigated. To the purpose, both numerical and experimental data will be used in a combined fashion.

4.1. Initial plunging phase and deck impact

Fig. 11 shows the initial plunging phase observed in the two-dimensional experimental investigation. Time increases from left to right and from top to bottom. For the same case, results (red lines) obtained by the described potential-flow model are superimposed. In particular, waves approach the obstacle from left to right. Some minor uncertainties in the comparison are introduced by wetting effects of the water on the lateral wall of the wave flume and to the angle of perspective. Nevertheless, the numerical simulations are in good agreement with the experimental visualizations. Further, despite surface-tension effects have not been modelled, the good comparison suggests a limited role of surface tension in determining the initial volume of the entrapped cavity, at least for the wave and the geometric parameters here considered.

The numerical free-surface configuration (solid line) at the impact instant is shown in the bottom-right plot of the same figure. It is also demonstrated that close to the separation point at the bow, the cavity profile is well fitted by the local solution [line with circles, cf. Zhao et al., 1997]. This approximation is obtained by neglecting gravity effects within the potential-flow approximation. The origin of the local coordinate system (x_1, z_1) is at the edge of the deck, with the

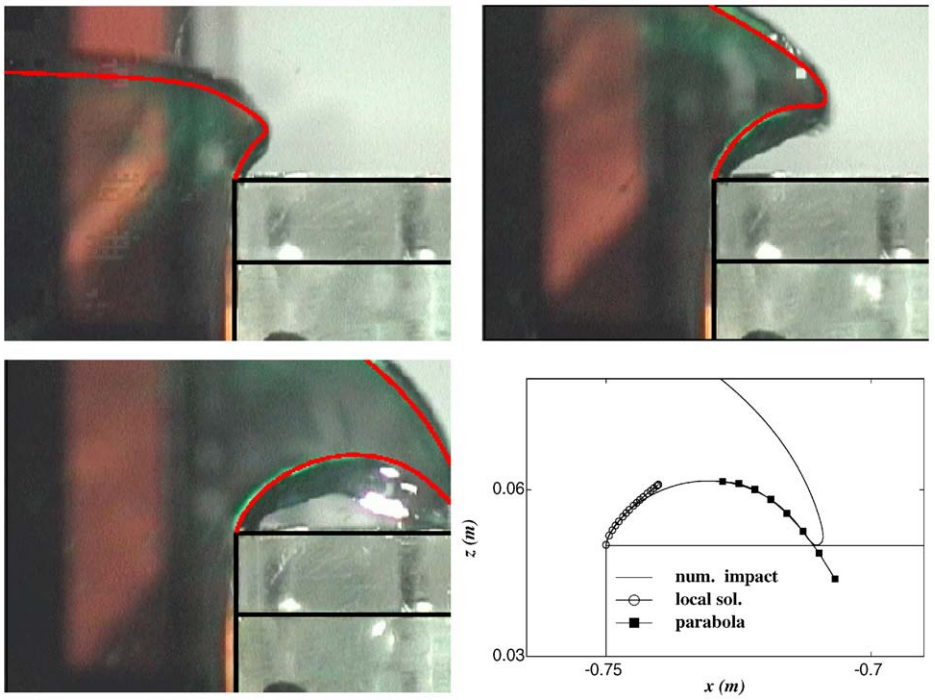

Fig. 11. Initial stages of water shipping on a two-dimensional structure caused by waves with $\lambda/D = 10.1$ and $H/D = 0.808$. The draft of the model is $D = 0.198$ m. The numerical results (red lines) are compared with experimental visualizations. The time interval between images is 0.04 s. Bottom right: the numerical solution (solid line) is compared with a local solution (line with circles) and with a free-falling trajectory (line with squares). Coordinates (x, z) have origin placed horizontally at the body center and vertically at the mean water level.

x_1-axis along the deck and the z_1-axis vertically upward. The coefficient $C(t)$ is a time varying parameter which depends on the complete flow, and therefore cannot be determined by a local analysis. The tip of the jet impacting against the deck agrees well with a parabolic contour (line with black squares), which would be the path of a free-falling fluid particle.

Therefore, at the beginning of the water shipping fluid particles undergo three stages of evolution: (i) the fluid is diverted vertically upward, with negligible effects of the gravity, (ii) an intermediate phase with almost horizontal motion where gravity and pressure gradients are comparable, and (iii) a free-falling evolution up to the impact against the underlying deck.

Considering the initial stage of water shipping from the structural loading point of view, the plunging phase is characterized by (i) the water impact against the deck, and (ii) the air-cushion phenomenon. In the following, the related effects on a ship deck are investigated. A real FPSO unit is considered to define the relevant structural parameters. In particular, the steel stiffeners along the selected FPSO deck are sketched in the left diagram of Fig. 12. The deck is designed to stand against a maximum spatially uniform pressure of 60 kPa. Within the present two-dimensional analysis, the structure in the longitudinal direction is modelled as an equivalent beam with cross-section sketched in the center plot of Fig. 12 and length $L_b = 2.5$ m.

It is assumed a full-scale draft of 18 m. Therefore, with the wave parameters mentioned above, the water-shipping and the related impact is caused by incident waves with length 182 m, and height 14.55 m. The free-surface configuration at the impact instant obtained by the numerical simulation for the equivalent two-dimensional problem is given in the right plot of Fig. 12. From the numerical simulation, an impact velocity of 4.3 m/s is estimated. This value is not large, and in particular is close to the orbital velocity in free-wave conditions (4.4 m/s). The free-surface shape near the initial impact position is rather blunt, and can be approximated by a circle with radius $r \simeq 0.1$ m. On a larger spatial scale, the plunging tip resembles a fluid wedge of about 20°, inclined of approximately 26° with respect to the vertical direction.

In the same figure, the two horizontal arrows indicate the length of the first two equivalent beams adopted to model the deck in the longitudinal direction. The impact starts close to the middle of the second one.

4.1.1. Water-impact loading

The loading evolution on the second beam b_2 is characterized by (i) an acoustic phase, (ii) a blunt-impact phase and (iii) a wedge-impact phase.

The water front at the impact instant can be approximated as a fluid circle hitting a flat wall. In the early stage, gravity effects can be neglected and the fluid–structure interaction can be studied by a Wagner-type approach. The corresponding model problem is sketched on the left-hand side of Fig. 13, where the main parameters involved are reported. In particular, the "wetted length" c can be obtained as $2\sqrt{Vrt}$ by locally approximating the initial circular shape of the fluid with a parabola. This approach cannot be used at the very beginning of the impact, when the method is not valid since the neglected water compressibility is important (acoustic phase), and infinite pressures are predicted. In reality, though high, the pressure cannot exceed the acoustic pressure $p_{ac} = \rho c_{s,w} V$. Here ρ is the water density, $c_{s,w}$ is the sound velocity in water (usually varying between 1450 and 1540 m/s), and V is the impact velocity. In the specific case, by using the impact velocity from the numerical simulation, we can estimate the maximum value of p_{ac} as $\sim$6.6 MPa. This is much larger than the design pressure. However since the high pressures are localized in space and time, the effect on the structure is limited. The time duration of the acoustic phase can be estimated through the Wagner method by imposing the maximum pressure, $p_{\max}$, equal to the acoustic value, p_{ac}, and assuming the impact velocity V remains constant during this stage, that is

$$\underbrace{\frac{\rho}{2}\left\{\frac{\mathrm{d}[c = 2\sqrt{Vt_{ac}r}]}{\mathrm{d}t}\right\}^2}_{p_{\max}} = \underbrace{\rho V c_{s,w}}_{p_{ac}} \quad \Rightarrow \quad t_{ac} = \frac{r}{2c_{s,w}}. \tag{15}$$

This gives $t_{ac} \sim 3.3 \times 10^{-5}$ s for the present case. Following Korobkin (1995), an estimate of the acoustic-phase duration is given by the condition $\mathrm{d}c_{\mathrm{geom}}/\mathrm{d}t = c_{s,w}$, where c_{geom} is the geometric intersection of the fluid circle with the deck after a penetration Vt. For very small times, by geometric arguments, we have $c_{\mathrm{geom}} = \sqrt{2Vrt}$ and therefore $t_{ac} \sim 0.9 \times 10^{-7}$ s. These two estimates give an indication of, respectively, the upper and the lower limit of the acoustic-phase duration t_{ac}, and show that this phase is quite short compared with the highest natural period of the equivalent beam b_2, $T_{d,1} = 0.0156$ s. Therefore, in spite of the relatively high pressure levels, this stage is not critical for the structural safety.

During the blunt-impact phase, for $t > t_{ac}$, a Wagner-type method can be used to find the evolution of the pressure distribution along the deck. The duration $t_{b.i.}$ of this second stage can be estimated as the time interval for half-circle of fluid to have impacted with the deck ($\beta = 90°$ in Fig. 13), from the end of the acoustic phase. In this case, by using the

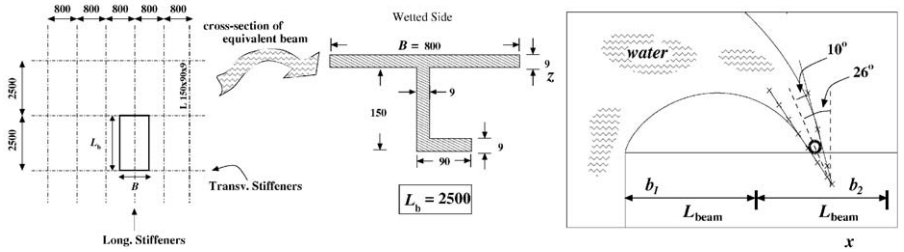

Fig. 12. Left: example of stiffeners arrangement in a FPSO deck (top view) Center: cross-section of the equivalent beam adopted to model the deck in the longitudinal direction. Dimensions are in millimeters. Right: numerical solution at the impact instant and its main global geometric parameters. The two horizontal arrows b_1 and b_2 indicate the length of the first and second equivalent beams along the deck, respectively.

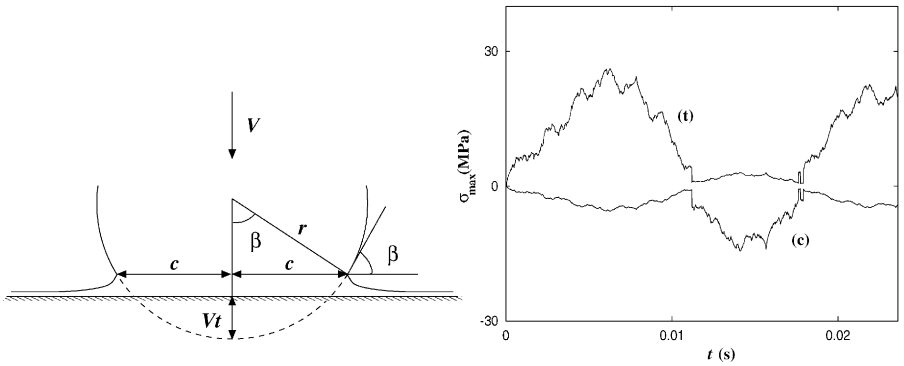

Fig. 13. Left: Sketch of the problem of a fluid circle hitting a flat horizontal wall. Right: evolution of the maximum tension (t) and compression (c) stresses along beam b_2 by assuming a Dirac's delta load. All quantities are given in full-scale ($D = 18$ m).

geometrical relationship $c = r\sin\beta$ and the solution $c = 2\sqrt{Vtr}$, we find $t_{b.i.} \sim 5.8 \times 10^{-3}$ s. At this time, the maximum pressure becomes 37 kPa, which is smaller than the design pressure. The time duration of the blunt-impact phase is larger than the acoustic-phase one, and corresponds to about 37% of the highest natural dry period $T_{d,1}$ of the equivalent beam b_2. Therefore, hydroelastic effects could matter and the elastic response of the beam has to be analyzed. In principle, a Wagner-type analysis is valid for small deadrise angles (Zhao and Faltinsen, 1993) say for $\beta \leqslant 20^\circ$. Since here we have used this approach up to $\beta = 90^\circ$ in combination with a parabolic approximation of the impacting free surface, we can expect that $t_{b.i.}$ has only been roughly estimated.

During the blunt-impact phase, the spatial region of the beam directly loaded by the fluid is of order $2r = 0.08L_b$, and therefore small relative to the beam length. Consistently, the beam evolution and the related stresses can be determined by considering the simplified problem of an initially undeformed simply supported beam subjected to a spatial Dirac-delta load, $f(t)\delta(x - x_{\text{imp}})$, at the initial impact position x_{imp}. The load amplitude $f(t)$ can be estimated as the vertical force on a rigid circle penetrating a flat free surface, Faltinsen (1990), and expressed as $\rho C_s(t) r V^2$. The time dependent coefficient C_s has been derived experimentally by Campbell and Weynberg (1980), and fitted by the formula

$$C_s = \frac{5.15}{1 + 8.5h/r} + 0.275\frac{h}{r}.$$

Here $h = Vt$ is the instantaneous submergence of the circle and is equal to r when half-circle penetrated the free surface. This means that the end of the blunt impact phase should be given by $t_{b.i.} = r/V \sim 2.44 \times 10^{-2}$ s which is four times the value predicted above. This value is not based on the assumption of small deadrise angle, and it should be considered a more realistic estimate than the previous one. The maximum stresses on the beam resulting from this analysis are presented in the right plot of Fig. 13 and remain safely below the yield stress (about 220 MPa).

The last stage of the fluid–structure interaction under analysis can be approximated by the impact of a fluid wedge of 20° hitting asymmetrically the deck. Upon assuming a rigid deck and that the impact velocity V remains constant, through the pressure analysis presented by Greco (2001) and based on the similarity solution from Zhang et al. (1996), we obtain a maximum pressure of about 18 kPa. This value is below the assumed structural safety limits for the deck.

4.1.2. Air-cushion loading

As observed in visualization and numerical studies, for the considered set of parameters the flow field on the deck closer to the bow is characterized by the cavity originated at the impact instant. During the evolution, the air cavity interacts with the surrounding fluid and undergoes deformations. As a consequence, the beam b_1, initially under the action of the atmospheric pressure, suffers loads due to the compressibility of the air entrapped in the cavity. If we assume a uniform pressure in the cavity, and we model the air evolution as the adiabatic process of an ideal gas, the pressure $p(t)$ in the cavity is related to the volume variations through

$$\frac{p(t)}{p_0} = \left\{\frac{\mathscr{V}_0}{\mathscr{V}(t)}\right\}^{\gamma} \quad \text{with } \gamma = 1.4. \tag{16}$$

Here, $p(t)$ and $\mathscr{V}(t)$ are the pressure and the volume at time t and p_0 and $\mathscr{V}_0$ are the corresponding reference values, e.g. the atmospheric pressure ($p_0 = 1$ atm $\simeq 10^5$ Pa) and the air volume in the cavity at the impact instant. The usual value $\gamma = 1.4$ is used for the ratio of the specific heats. Any flow in the air preceding the cavity closure is neglected and Froude scaling is assumed to transfer the data from model to full-scale conditions.

By using the above model and the digital images taken from the experiments, we have carried out an analysis to evaluate the pressure acting on the first beam. In the sequence of Fig. 14, the post-impact evolution is shown with snapshots separated in time by an interval of 0.38 s (full-scale). The cavity profile is not sharply detectable from the pictures because of camera resolution limits, wetting effects of the lateral wall and perspective errors. Therefore, for each snapshot several different curves are candidates as cavity boundary. All of them have been considered and are reported, superimposed to the corresponding video image. From such images the cavity volume $\mathscr{V}(t)$ has been evaluated and different results have been obtained because of the uncertainty in the determination of the cavity boundary. The initial cavity volume $\mathscr{V}_0$ has been computed from the numerical simulation of the same wave conditions. Once the preliminary analysis has been completed, we can compute the pressure evolution inside the cavity by (16).

The circles in the bottom-right plot of Fig. 14 represent the pressure computed according to the above procedure. As anticipated, different values at the same time instant are obtained, corresponding to different digitized cavity boundaries. The pressure envelope (dashed lines) gives an indication of the order of magnitude of the uncertainty involved in. The horizontal solid line is the design pressure for the deck and, according to the present analysis, this value

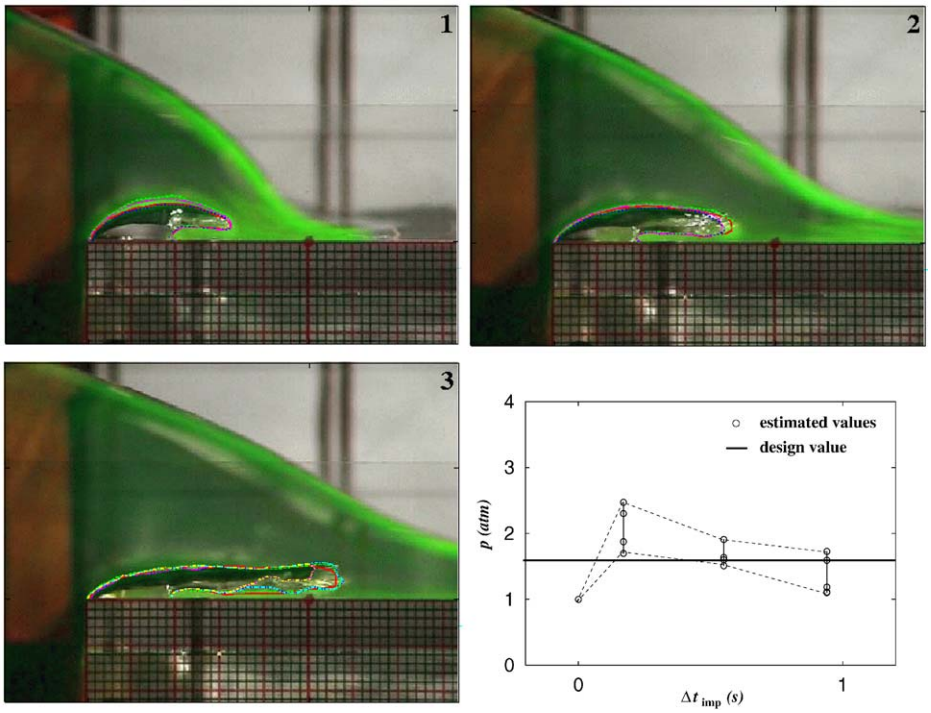

Fig. 14. Air-cushion phenomenon at the bow edge induced by waves with $\lambda/D = 10.1$ and $H/D = 0.808$. Snapshots 1–3: visualization of the air-cavity evolution. Referred to the full-scale draft $D = 18$ m, the time interval between two following frames is 0.38 s. The digitized cavity profiles (colored lines) are superimposed to the images. Bottom right: pressure evolution inside the cavity.

can be exceeded during the cavity evolution. Therefore, the collapse of the cavity can be critical for the strength of the deck structure. At full scale, the time duration of the "loading cycle" due to the air-cushion phenomenon is order of 1 s and it is much longer than the first dry natural period of the beam b_1, $T_{d,1} \simeq 0.0156$ s. This suggests that hydroelastic effects are not relevant.

In this analysis, to define the initial conditions for full-scale draft, Froude scaling has been assumed and the influence of viscous and surface-tension effects have been neglected. Similarly, the influence of air motion in determining the water evolution *before* the cavity formation has been neglected. Another approximation in scaling the results is related to the cavity evolution *after* its formation which is influenced by the Euler or cavitation number $Eu = (p_a - p_v)/(\rho V^2)$. In particular, upon neglecting the role of the vapor pressure p_v, we can assume that the initial air-pocket pressure is always of the order of the ambient (atmospheric) pressure p_a, while the impact velocity V of the wave front plunging onto the deck changes according to the geometrical scale considered, and extrapolation from model scale to full scale can be more uncertain. Dynamic effects in the cavity pressure evolution are also neglected.

In a different context Greco et al. (2003), studying the air-cushion following wave impact on the bottom of a floating structure, numerically found that if the cavitation number is large enough, say $Eu \sim \mathcal{O}(10^3)$, then the evolution of the entrapped cavity can be qualitatively different and the air tends to escape. For $Eu \leqslant \mathcal{O}(10^2)$, the short-time evolution of the air cavity is similar to that observed in the present experiments and the extrapolation to full scale seems qualitatively plausible, though probably too conservative.

It should be finally mentioned that in three-dimensional conditions air could find ways to escape before entrapment and cushion phenomena appear. In the recalled three-dimensional model experiments, Barcellona et al. (2003), air entrapment has been still observed, though with more complex cavity geometries, leaving open the need of a fuller understanding and quantitative prediction of this phenomenon.

4.2. Deck-house impact

On a longer time scale, the observed water shipping resembles a dam-break type phenomenon. That is the fluid runs along the initially dry deck without significant overturning phenomena at the water front, and the fluid-dynamic regime is practically of shallow-water type. During this dam-break stage, our numerical and physical experiments show that the loading is mostly determined by the 'hydrostatic' pressure, since ship motions have been restrained. Actually, additional contributions are due to three-dimensional effects and deck accelerations. This phase is not expected to be dangerous for the deck structure although, depending on the amount of shipped water, it can be relevant for the dynamic behavior of the ship. This issue is not addressed here.

Fig. 15 shows the evolution of the shipped water during the dam-break stage, in the absence of vertical superstructures. In the left frame, it is visible that the air cavity, formed during the early stage of the water shipping, is now highly deformed and left far behind the fluid front. Therefore, it is expected that the presence of air bubbles is not influencing significantly the gross evolution of the flow field during the considered stage. Indeed, this is confirmed by the good comparison with the numerical simulation (red lines in the figure) obtained by neglecting the entrapped air and enforcing the "initial" Kutta condition. Similar agreement is found during the whole evolution, including the late stages when the water shipping finally ceases, as reported in the right frame of Fig. 15.

On this ground, at least for the considered two-dimensional cases, we can state that the main features both of the deck flow and of the impact flow on the superstructures are not affected by the details of the initial plunging phase. This also implies that a potential-flow scheme without modelling of the entrapped air bubbles can give useful information about the impact-flow stage. This is better shown in Fig. 16, where the experimental visualizations are compared with the numerical free-surface profiles in the case of a vertical wall located at 0.2275 m from the bow of the model.

Fig. 17 provides a closer view of the water front approaching the vertical superstructure. It resembles a thin half-wedge, left picture, and at the beginning of the impact only the small amount of the fluid sharply deviated upward is affected by the phenomenon. A vertical jet is originated and spray formation is observed. Though the description of spray and interface fragmentation is beyond the possibility of the present potential flow model, these details have a limited dynamic role on the resulting loads. On the contrary, during this initial stage, even a simpler zero-gravity model can provide a good approximation to the flow, as documented by Faltinsen et al. (2002) where the similarity solution from Zhang et al. (1996) is extended to give the initial pressure distribution on the wall and analytical formulae for estimating the maximum impact pressure are provided.

The pressure evolutions on the wall have been measured at three locations by piezoelectric transducers, with 3 mm diameter. This means the evaluated pressure is an averaged value over a small area of about 7 mm^2. During the tests we adopted a sampling frequency of 200 Hz. Two pressure transducers, PG1 and PG2, are located at 0.012 m and at 0.032 m above the deck (model scale), respectively. The third transducer, PG3, is at the same height of PG1 but 0.15 m shifted in the transverse direction. Typical pressure evolutions are reported in Fig. 18. In the same figure, the pressure

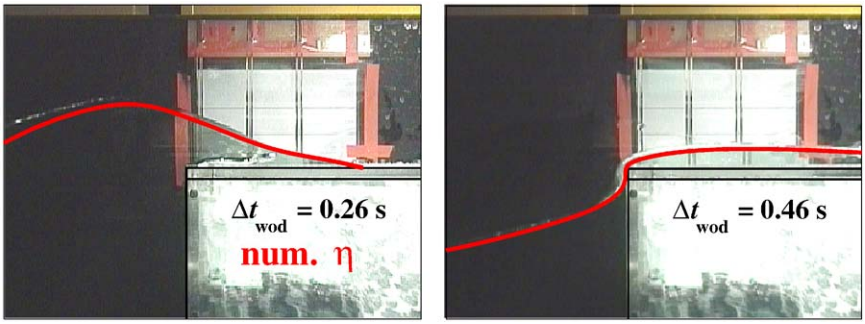

Fig. 15. Dam break-type stage of the water shipping induced by waves with $\lambda/D = 10.1$ and $H/D = 0.808$. The red lines are the present numerical simulations and the time intervals Δt_{wod} after the water shipping are referred to the experimental conditions, $D = 0.198$ m. For a full-scale draft $D = 18$ m, the corresponding time instants from the water shipping starting, Δt_{wod}, are 2.480 and 4.36 s, respectively.

Fig. 16. Impact of the shipped water against a vertical superstructure located at 0.2275 m from the model bow. Water shipping is induced by waves with $\lambda/D = 10.1$ and $H/D = 0.808$. Red lines are the present numerical simulations. Time increases from left to right: time instants from the water shipping starting $\Delta t_{wod} = 0.273$, 0.313 and 0.353 s (2.603, 2.984 and 3.366 s full-scale draft $D = 18$ m).

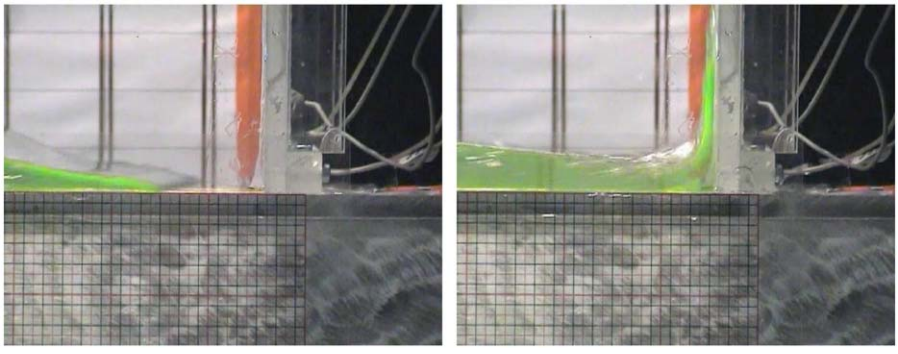

Fig. 17. Water impact against a vertical wall after water shipping caused by waves ($\lambda/D = 10.1$ and $H/D = 0.808$). Enlarged view of the thin-wedge shaped water front before the impact (left) and after the impact (right).

computed numerically is also presented (thick solid line). The origin of the time scale corresponds to the time instant when the numerical pressure at the lowest gauge location attains a nonzero value.

Left and center plots show the pressure measured by PG1 and PG2, respectively. For the former, the pressure rises quite sharply, reaches a maximum value $p_{max,1}$, and then decreases, with some oscillations. After the minimum is attained, a second steep increase is observed up to the peak $p_{max,2}$. The rise time of the two loading cycles as well as the

pressure peaks are comparable, though $p_{max,2} < p_{max,1}$. A similar qualitative behavior is observed for the transducer PG2, although in this case the first maximum is smaller than the second one and it is reached in a slightly longer rise time.

The first pressure cycle is associated with the initial water impact against the superstructure. The second one is related to the backward water overturning, shown in Fig. 7, as we found by combining the pressure measurements with the video images. More in detail, it is connected with the impact of the backward plunging wave with the underlying mass of water. Being of comparable order of magnitude, both loading cycles appear equally important for the structural safety. This behavior has been confirmed by the three-dimensional model tests described by Barcellona et al. (2003), where the pressure distribution on the deck and the horizontal fluid force on a vertical wall at its end have been measured (cf. Fig. 21 and 22 in Barcellona et al., 2003). Clearly, in three-dimensional cases, the water can flow off the deck and the mass involved in the backward overturning can be smaller, possibly reducing the strength of the second loading cycle. Yet, the second pressure peak along the ship center-line was always found comparable to the first one.

The numerical prediction is rather satisfactory and recovers correctly the first pressure peak. Though the computations could have been continued up to the backward-plunging water front impinges onto the underlying free surface, the second pressure peak would not be numerically captured anyway because the boundary element method cannot handle free-surface breaking. In this respect, Level Set (Colicchio et al., 2002), SPH (Colagrossi and Landrini, 2003) and VOF (Greco et al., 2002) techniques have been applied to similar problems to handle the post-breaking evolution but further development and validation for extensive and practical use in this context are required.

We note that two test results are reported for each pressure gauge and show a not-perfect repeatability. During first tests, variations of pressure have been found due to temperature changes induced by passing from dry to wet conditions. This bias error has been reduced by keeping (roughly) constant the transducers temperature in between two following tests simply by covering them with a wet towel. Yet, though qualitatively similar, pressure evolutions show some scatter. Actually, the data comparison (right diagram in Fig. 18) for transducers PG1 and PG3 located at the same height from the deck highlights differences of the same order of the data scatter observed from repetition tests. This observation, supported by the flow images in Fig. 19, suggests that three-dimensional effects appearing soon after the impact are the major responsible for the observed behavior.

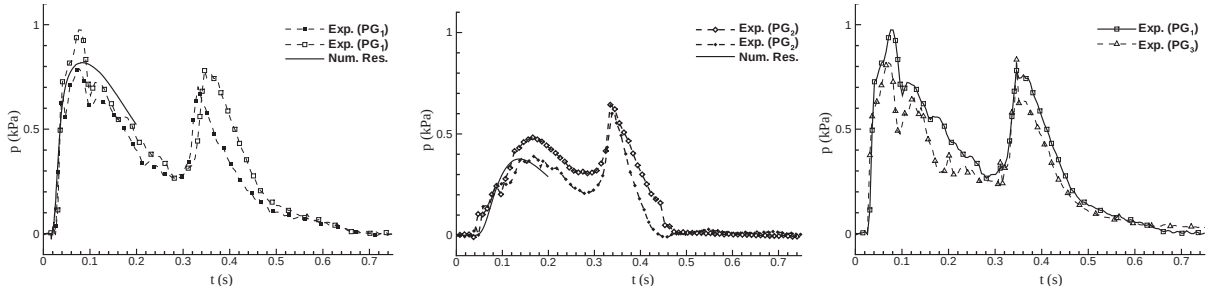

Fig. 18. Pressure evolution measured on the vertical wall under impacting conditions, at 0.012 and 0.032 m above the deck (left and center plots, respectively). Two test results are given for each gauge location. The solid lines give the numerical results before breaking occurs.

Fig. 19. Three-dimensional instabilities of the water front during the run up after the impact. Left: back view. Right: front view.

Further observation of the pressure evolutions evidences some high-frequency oscillations, visible during the first loading cycle, and possibly related to arriving air bubbles entrapped at the bow edge. In any case, the available images and the sampling frequency adopted in pressure measurements do now allow for a better insight into these details.

4.3. Hydroelastic effects

During the most impulsive stages, if the loading time is comparable with the structural natural wet period, hydroelasticity is excited, and for a correct structural design its effects should be assessed. In the following, the influence of hydroelasticity during the water impact with vertical superstructures is investigated. Inflow conditions are generated by an equivalent dam-break problem (cf. left plot of Fig. 20), and the resulting fluid–structure interaction is analyzed by using the hydroelastic model of Section 3.4.

The sketches in Fig. 20 gives an example of typical longitudinal steel stiffeners adopted for the deck house in the bow region of a FPSO. Attention is focused on stiffeners between decks 8 and 9 shown in the figure. This is done by using an equivalent Euler beam, with the cross section represented in the bottom right of the same figure. The upper portion of the deck house is assumed rigid.

Recent documented casualties for FPSO units suggest to use a freeboard exceedance of 10 m. We therefore assumed an equivalent problem consisting in a breaking dam located at the bow section, with a water reservoir $h = 10$ m high and $2h$ long (cf. Fig. 20). Consistently with operating FPSO units, the beam representing the deck house wall is located at $d_s = 2.139h$ from the dam, with length $L_b = 0.311h$. The lower edge is clamped, while rotations at the upper edge are constrained by a spring with elastic constant k_θ.

Fig. 20 shows the initial condition and a later free-surface configuration when the water front has already impacted with the deck house. Here and in the following, time is made nondimensional by $\sqrt{h/g}$. For the considered initial conditions, the impact instant is $\tau_{\text{imp}} = 1.705$. The time interval for the beam to be completely wetted is about $\Delta\tau_{\text{imp}} = \tau - \tau_{\text{imp}} = 0.12$ and is practically unaffected by the beam deformations. Also, the typical time for the total force acting on the beam to reach its maximum value is about $\Delta\tau_{\text{imp}} = 0.27$, after that the force decays. Therefore, all cases treated in the following refer to a time scale of about $\Delta\tau_{\text{imp}} = 0.3$ after the impact.

The numerical solution can be negatively affected by a variety of difficulties. For instance spatial and time resolutions decrease progressively for higher-order modes. Confluence of different boundary conditions at the edges of the beam implies locally a poorer convergence. Invariance of the solution by doubling the initial number of panels and halving the initial time step has been verified. Fifteen modes have been found to guarantee at convergence on the most significant modes.

A simplified analytical analysis (sketched in Fig. 21) is also performed to qualitatively verify the present results. The water domain is approximated by a strip of fluid with constant height H, and the potential φ_j is due to the jth oscillation mode with unit amplitude. The condition $\varphi_j = 0$ is applied along the free surface. The analytical solution is found by separation of variables and Fourier expansion technique. The height H is a free parameter, and it is chosen as follows. In the approximate problem, it is found that the fluid further away than $\sim 0.8L_b$ from the beam is practically unaffected by the beam vibrations. Therefore, H is determined by imposing that masses of fluid involved in the approximate and exact problems are the same, and the value $H/h = 0.207$ has been obtained. Though there is some arbitrariness in this procedure, the objective is to show that the numerical results behave reasonably. The table in Fig. 21 shows the ratios of the natural wetted period $T_{w,j}$ to the natural dry period $T_{d,j}$ by the "exact" and approximate problems, respectively. The comparison, tabulated for $j = 1, 2, 3$ and for $k_\theta = 0, \infty$, shows a reasonable agreement, which improves for the higher modes as one can expect since their sensitivity to the fluid details is smaller.

We now discuss in more detail the results obtained by the numerical solution of the exact hydroelastic problem. Fig. 22 shows the time evolution of the beam deformation in terms of the amplitudes ζ_j of the first four modes for $k_\theta = 0$. The evolutions of the first two modes are shown in the left diagrams, while only the late stages of the first four modes are shown in the right plots. For $j = 1, 2$, ζ_j oscillates around a mean value which grows in time. The oscillation amplitude becomes nearly constant after the beam becomes completely wetted. A similar behavior could be observed for higher modes, though the mean value and the oscillation amplitude decrease for increasing j. In reality, structural damping may affect higher-mode evolutions, but this effect has not been considered here.

The qualitative behavior of the solution does not change significantly by varying the parameter $K_\theta = k_\theta L_b/EI$. In particular, as K_θ increases the amplitudes decrease. The influence appears minor for the higher modes which are less sensitive to the boundary conditions. In general, the ratio $T_{w,j}/T_{d,j}$ of natural wetted period to natural dry period decreases as K_θ increases and is smaller for higher j (see Table 1). The highest natural wetted-period $T_{w,1}\sqrt{g/h}$ changes from 0.018 to 0.026 for K_θ in the range $[\infty, 0]$. Therefore, $T_{w,1}$ is small relative to typical loading time, $\Delta\tau_{\text{imp}} = 0.27$. This suggests a limited role of hydroelasticity.

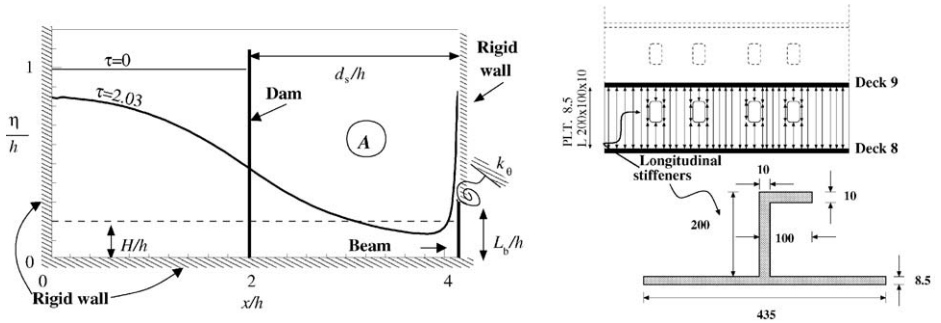

Fig. 20. Left: flow impacting with a vertical flexible wall after the breaking of a dam. Sketch of the problem and nomenclature adopted. The main parameters adopted in the simulation are $L_b/h = 0.311$, $d_s/h = 2.139$ and $h = 10$ m. Nondimensional time $\tau = t/\sqrt{h/g}$. Right: example of stiffeners of a deck house (front view on the top) and cross-section of equivalent beam. Lengths are in millimeters.

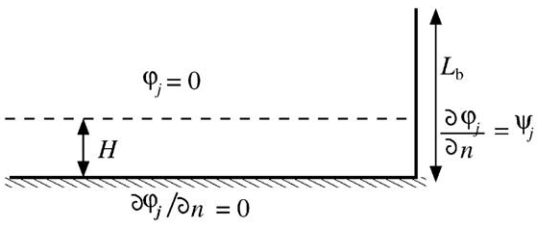

	j	Exact	Approximate
$k_\theta = 0$	1	2·74	2·20
	2	2·26	2·34
	3	1·93	1·96
$k_\theta = \infty$	1	2·67	2·50
	2	2·22	2·20
	3	1·88	1·87

Fig. 21. Wetted natural periods. Left: sketch of the simplified problem. Right: ratios $T_{w,j}/T_{d,j}$ obtained by the "exact" fully numerical solution and by the approximate analysis for two different spring stiffness k_θ.

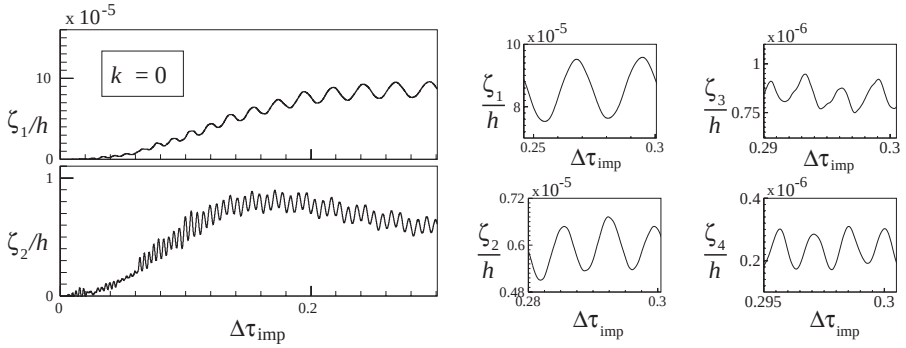

Fig. 22. Modal amplitude as a function of time. Left: time evolution of the first two modes. Right: enlarged view of the amplitude of the first four modes at large times after the impact.

Table 1
Ratio of natural wetted-periods to natural dry-periods for the first four modes of the beam. $K_\theta = k_\theta L_b/EI$

	K_θ			
j	0	6	24	∞
1	2.74	2.73	2.67	2.67
2	2.26	2.25	2.23	2.22
3	1.93	1.93	1.88	1.88
4	1.71	1.70	1.67	1.67

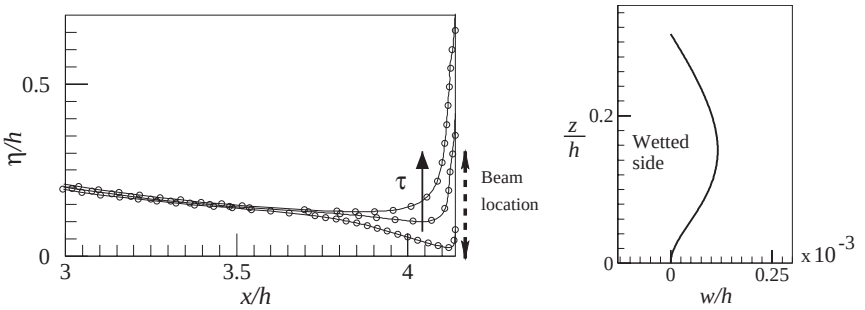

Fig. 23. Left: free surface configurations for $\Delta\tau_{imp} = 0.024,\ 0.13,\ 0.24$ after the impact; solid lines: rigid wall, ◦: hydroelastic solution with $k_\theta = 0$. Right: beam deformation for $k_\theta = 0$ and $\Delta\tau_{imp} = 0.12$ after the impact.

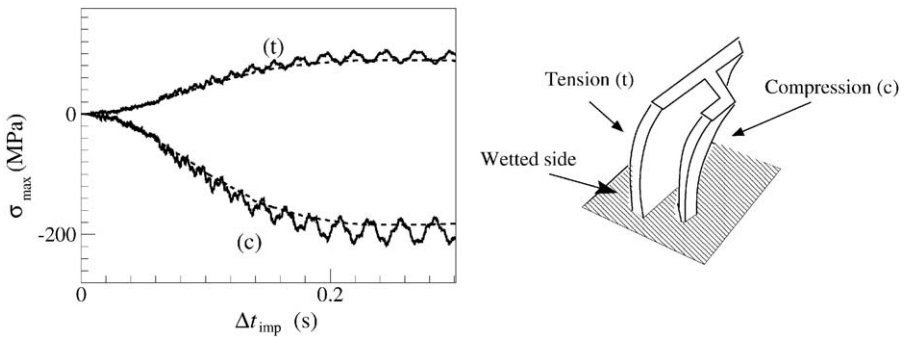

Fig. 24. Left: evolution of the maximum tension (t) and compression (c) stresses for $k_\theta = 0$. Right: sketch of the loaded beam.

Moreover, the free-surface evolution is practically unaffected by the beam oscillations. Fig. 23 compares the free-surface configurations in case of rigid-wall (solid lines) against the results obtained by the hydroelastic model for a clamped–supported beam, ◦. The results are graphically superimposed. An example of the instantaneous deformation of the beam is given on the right of the same figure.

To further assess the role of hydroelasticity, the maximum stresses $\sigma_{\max}$ on the beam computed in the present hydroelastic analysis are compared with those evaluated by a quasi-steady model. In the latter, a rigid structure is considered in the solution of the hydrodynamic problem, and the resulting loads are used to compute the static structural deformation. For the considered cases, maximum stresses are always observed at the bottom end. In particular, the fluid-induced bending moment gives tension stresses (t) in the wetted side, and compression stresses (c) in the opposite side, cf. the right plot in Fig. 24. Compression bending stresses reach larger values than tension stresses because the cross-sectional neutral axis is closer to the wetted side. After the transient stage, the mean value of $\sigma_{\max}$ becomes nearly constant and remains with an absolute value less than 220 MPa, which is smaller than the steel yield stress. The magnitude of hydroelastic results oscillates around a mean value close to and slightly larger than the corresponding quasi-steady value. This confirms, for the considered case, the limited role of hydroelasticity.

5. Conclusions

The bow water shipping for a two-dimensional structure in head sea and restrained from moving has been studied by experimental and numerical means. The main stages of the flow-field evolution have been highlighted and the related loading regimes have been addressed.

For the considered cases, it is found that water shipping starts with the fluid front plunging onto the deck and entrapping air in cavities of complex shape and evolution. This behavior can be successfully described by a potential flow model with a suitable Kutta-type condition at the bow edge. A simplified analysis of two-dimensional experimental data shows that this air-cushion stage can lead to high pressure (very localized in space and time), and therefore to possible structural damages.

After the cavity disintegration, the following dam break-like evolution is grossly unaffected by the presence of the air bubbles dispersed within the main bulk of water. Numerical simulations, where the presence of air bubbles has been neglected, reproduce well the overall flow scenario and can be used to compute the initial conditions to study the impact against deck structures.

In this context, shallow-water models may be useful although the need of boundary data may pose severe limitations to their actual applicability, as discussed by Greco (2001). This stage is probably more relevant to the dynamics of the vessel rather than to the strength of the deck.

The impact against vertical deck structures is finally addressed. Although the impact loads are of main importance, laboratory measurements have shown that pressure peaks arising during the gravity-driven evolution can be of the same order of magnitude and, therefore, of concern for design purposes. In this framework, the potential-flow modelling has been proved reliable to simulate the flow and to predict the hydrodynamic loads at least up to breaking and fragmentation of the free surface occur. Within the first stage, even more simplified tools have been proposed by Faltinsen et al. (2002) which can be easily used for design and certification purposes. In the breaking regime, new strategies of numerical simulations are under development (e.g. Greco et al., 2002; Colicchio et al., 2002; Colagrossi and Landrini, 2003), where field methods based on either Euler or Navier–Stokes equations are used to handle free surface fragmentation and breaking. In this context a domain decomposition (DD) strategy, to extend the analyses performed by the boundary element method, is investigated. Within the DD, a field method with a more general treatment of the free-surface should be introduced in domain regions where breaking and two-phase flows are observed, while the BEM would be applied in the rest of the fluid domain. This approach would partially retain BEM advantages in terms of efficiency and accuracy in describing free-surface flows. Further, it would be more general than the BEM in terms of prediction of water shipping occurrence and study of the phenomenon along the whole flow evolution along the deck, avoiding for instance the need of using different Kutta-like conditions at the edge of the deck.

Finally, the numerical model has been extended to deal with hydro-elastic problems. The method was found stable and relatively efficient and it has been verified by using some simplified analytical solutions. Then, the impact of shipped water against the vertical wall of a deck-house has been studied. An equivalent dam-break problem has been adopted to generate the inflow conditions and tuned by using data of recent casualties. Structural parameters have been deduced from a really operating FPSO unit. For the considered data set, it was shown that hydroelasticity is of minor importance and that a quasi-steady structural analysis is enough for design purposes, leaving to the hydrodynamic analysis the major responsibility to predict the fluid loading history.

References

Barcellona, M., Landrini, M., Greco, M., Faltinsen, O., 2003. An experimental investigation on bow water shipping. Journal Ship Research 47 (4), 327–346.

Buchner, B., 1995. On the impact of green water loading on ship and offshore unit design. In: Proceedings International Symposium Practical Design of Ships and Mobile Units, PRADS'95, Seoul, The Society of Naval Architects of Korea, pp. 430–443.

Buchner, B., 2002. Green water on ship-type offshore structures. Ph.D. Thesis, Technical University of Delft, Delft, Holland.

Buchner, B., Cozijn, J.L., 1997. An investigation into the numerical simulation of green water. In: Proceedings International Conference on the Behaviour of Offshore Structures, BOSS'97, Delft, Vol. 2. Elsevier, Amsterdam, pp. 113–125.

Campbell, I.M.C., Weynberg, P.A., 1980. Measurement of parameters affecting slamming. Final report. Technical Report 440, Technology Reports Centre No. OT-R-8042, Wolfson unit for marine technology, Southampton University.

Clément, A., 1996. Coupling of two absorbing boundary conditions for 2d time-domain simulations of free surface gravity waves. Journal of Computational Physics 126, 139–151.

Cointe, R., 1989. Nonlinear simulation of transient free surface flows. In: Proceedings of Fifth Symposium on Numerical Ship Hydrodynamics, pp. 239–250.

Colagrossi, A., Landrini, M., 2003. Numerical simulation of interfacial flows by smoothed particle hydrodynamics. Journal of Computational Physics 191, 448–475.

Colicchio, G., Landrini, M., 2003. On the use of boundary integral equation methods for unsteady free-surface flows. Journal of Engineering Mathematics (46), 127–146.

Colicchio, G., Colagrossi, A., Greco, M., Landrini, M., 2002. Free-surface flow after a dam break: a comparative study. Ship Technology Research 49 (3), 95–104.

Dommermuth, D.G., Yue, D.K.P., 1987. Numerical simulations of nonlinear axisymmetric flows with a free surface. Journal of Fluid Mechanics 178, 195–219.

Ersdal, G., Kvitrud, A., 2000. Green water on Norwegian production ships. In: Proceedings 10th International Conference Offshore and Polar Engineering, ISOPE'2000, Seattle, paper No. 2000-IL-01, pp. 1–8.

Faltinsen, O., 1977. Numerical solutions of transient nonlinear free-surface motion outside or inside moving bodies. In: Wehausen, N.S.J.V. (Ed.), Proceedings of the Second International Conference Numerical Ship Hydrodynamics, Berkeley, USA, pp. 347–357.

Faltinsen, O.M., 1990. Sea Loads on Ships and Offshore Structures. Cambridge University Press, Cambridge, UK.
Faltinsen, O., Greco, M., Landrini, M., 2002. Green Water Loading on a FPSO. ASME/Journal of Offshore Mechanics and Arctic Engineering 124, 1–7.
Fekken, G., Veldman, A.E.P., Buchner, B., 1999. Simulation of green water loading using the Navier-Stokes equations. In: J. Piquet (Ed.), Proceedings of the Seventh International Conference Numerical Ship Hydrodynamics, Nantes, France, pp. 6.3-1–6.3-9.
Greco, M., 2001. A two-dimensional study of green-water loading. Ph.D. Thesis, Department of Marine Hydrodynamics, NTNU, Trondheim, Norway.
Greco, M., Faltinsen, O.M., Landrini, M., 2002. Water shipping on a vessel in head waves. In: Proceedings 24th Symposium on Naval Hydrodynamics, Technical session: Slamming, Green Water and Capsizing, Fukuoka, Japan, pp. 1–14.
Greco, M., Landrini, M., Faltinsen, O.M., 2003. Slamming and water shipping on a VLFS with shallow draft. In: Proceedings 18th International Workshop on Water Waves and Floating Bodies, Le Croisic, France, Paper No. 18, pp. 1–4.
Israeli, M., Orszag, S., 1989. Approximation of radiation boundary conditions. Journal of Computational Physics 41, 115–135.
Kleefsman, K.T., Fekken, G., Veldman, A.E., Bunnik, T., Buchner, B., Iwanowski, B., 2002. Prediction of green water and wave loading using a Navier–Stokes based simulation tool. In: Proceedings 21st International Conference Offshore Mechanics and Artic Engineering, Norway, Paper No. 28480, pp. 1–8.
Korobkin, A., 1995. Acoustic effects on water impact. In: Proceedings 10th International Workshop of Water Waves and Floating Bodies, Oxford, UK, pp. 125–128.
Kvålsvold, J., 1994. Hydroelastic modelling of wetdeck slamming on multihull vessels. Ph.D. Thesis, Norwegian Institute of Technology, NTH, Trondheim, Norway.
Landrini, M., Grytøyr, G., Faltinsen, O.M., 1999. A B-Spline based BEM for unsteady free surface flows. Journal Ship Research 43 (1), 1–12.
Longuett-Higgins, M.S., Cokelet, E.D., 1976. The deformation of steep surface waves on water. I A numerical method of computation. Proceedings of the Royal Society of London A 350, 1–26.
Ogilvie, T.F., 1967. Nonlinear high-Froude-number free surface problems. Journal of Engineering Mathematics 1, 215–235.
Rappi, R.J., Melville, W.K., 1990. Laboratory measurements of deep-water breaking waves. Philosophical Transactions of the Royal Society of London A 331, 735–800.
Salvesen, N., Tuck, E.O., Faltinsen, O.M., 1970. Ship motions and sea loads. Transactions SNAME 78, 250–287.
Stansberg, C., Karlsen, S., 2001. Green sea and water impact on FPSO in steep random waves. In: Proceedings 21st Symposium on Practical Design of Ships and Mobile Units, PRADS'2001, Shanghai, China, pp. 593–601.
Tanizawa, K., 1999. A numerical simulation method of hydroelastic water surface impact based on acceleration potential. In: Proceedings 3rd ASME/JSME Joint Fluids Engineering Conference, FEDSM99, San Francisco, Paper No. 6908, pp. 1–10.
Yeung, R.W., 1982. Numerical methods in free-surface flows. Annual Review of Fluid Mechanics (14), 395–442.
Zhang, S., Yue, D.K.P., Tanizawa, K., 1996. Simulation of plunging wave impact on a vertical wall. Journal of Fluid Mechanics 327, 221–254.
Zhao, R., Faltinsen, O.M., 1993. Water entry of two-dimensional bodies. Journal of Fluid Mechanics 243, 593–612.
Zhao, R., Faltinsen, O.M., Aarnes, J., 1997. Water entry of arbitrary two-dimensional sections with and without flow separation. In: Proceedings 21st Symposium on Naval Hydrodynamics, National Academy Press, Trondheim, Norway, pp. 408–423.